Title
A biomimetic eye with a hemispherical perovskite nanowire array retina

Journal
Nature, 581(7808)

ISSN
0028-0836

Authors
Gu, Leilei
Poddar, Swapnadeep
Lin, Yuanjing
et al.

Publication Date
2020-05-21

DOI
10.1038/s41586-020-2285-x

Peer reviewed

Biomimetic Electrochemical Eye with Hemispherical Perovskite Nanowire Array Retina

Leilei Gu[1], Swapnadeep Poddar[1], Yuanjing Lin[1, 2], Zhenghao Long[1], Daquan Zhang[1], Qianpeng Zhang[1], Xiao Qiu[1], Matthew Kam[1], Ali Javey[2, 3], Zhiyong Fan[1*]

[1]Department of Electronic and Computer Engineering, The Hong Kong University of Science and Technology, Clear Water Bay, Kowloon, Hong Kong SAR, China

[2]Electrical Engineering and Computer Sciences, University of California, Berkeley, California 94720, United States

[3]Materials Sciences Division, Lawrence Berkeley National Laboratory, Berkeley, CA 94720, USA

*Correspondence to: eezfan@ust.hk

Human eyes possess exceptional image sensing characteristics such as spectacularly wide field of view (FOV), high resolution and sensitivity with low aberration. Biomimetic eyes with the same superior characteristics are highly desirable in many technological applications. However, the spherical nature of biological eyes, particularly the core component of retina, poses an enormous challenge for fabrication of biomimetic eyes. Herein, we demonstrate a unique biomimetic electrochemical eye using a hemispherical retina made of high-density array of nanowires mimicking photoreceptors on a real retina. The device design has a high degree of structural similarity to a real human eye with potency to achieve a high imaging resolution when individual nanowires are electrically addressed. Meanwhile, image sensing function of our biomimetic eye device is also demonstrated. The work here may lead to a new generation of photosensing and imaging devices based on a bioinspired design that can benefit a wide spectrum of technological applications.

Biological eyes are arguably the most important sensing organ for most of the animals on this planet. In fact, our brain acquires more than 80% of information about our surroundings via our eyes, in addition to other senses[1]. A human eye with a concavely hemispherical retina and light-management components is particularly notable for its exceptional characteristics including wide FOV of up to 150^{o}, high resolution of 1 arcmin per line pair at the fovea and excellent adaptivity to the optical environment[2]. Particularly, the dome shape of retina has the merit of reducing optical systems' complexity by direct compensating the aberration from curved focal plane (*i. e.*, Petzval surface)[3]. Similar to human eyes, artificial vision systems play the same important role in autonomous technologies such as robotics. Particularly for humanoid robots, the vision system is supposed to resemble that of human in appearance to enable amicable human-robot interaction, in addition to having superior device characteristics, such as high sensitivity, high resolution, low aberrations, *etc*. In principle, a hemispherical image sensor design mimicking that of human retina can achieve this goal. However, the commercial charge-coupled device (CCD) and complementary metal-oxide-semiconductor (CMOS) image sensors are dominantly using planar device structures shaped by the mainstream planar microfabrication processes which is hardly possible for hemispherical device fabrication.

Herein, we demonstrate an artificial visual system using successfully assembled spherical biomimetic electrochemical eye (EC-EYE) with hemispherical retina made of a high-density perovskite nanowire (NW) array grown by vapor-phase approach. Ionic liquid electrolyte was used as a front side common contact to the NWs and liquid metal wires were used as back contacts to NW photosensors mimicking human nerve fibers behind the retina. Device characterization indicates that the EC-EYE has a high responsivity, reasonable response speed, low detection limit as well as wide FOV. The EC-EYE also demonstrates the basic function of a human eye to acquire

image patterns. In addition to structural similarity with a human eye, the hemispherical artificial retina has NW density (4×10^8 cm^{-2}) much higher than that of photoreceptors in a human retina thus can potentially achieve a higher image resolution. To demonstrate this potency, a single-NW ultra-small photodetector with footprint ~0.22 μm^2 has been fabricated and characterized.

Figure 1 shows the schematic comparison of a human (Fig. 1a) and our EC-EYE imaging systems (Fig. 1b). As illustrated by Fig.1a1, the human visual system is a comprehensive system consisting of two eye bulbs for optical sensing, millions of nerve fibers for data transmission and brain for data processing. A human brain has a spectacular capability of parallel processing thus signals from ~1 million nerve fibers can be processed at the same time, and image processing and recognition can be implemented in a very short time[4]. The detailed structure of a human eye is shown in Fig. 1a2, which has a lens, a spherical cavity and a hemispherical retina. In this structure, the retina is the core component to convert optical images to neuroelectric signals that can be processed by the brain. Its hemispherical shape simplifies eye optical design resulting in extraordinarily large FOV of ~155^o with a wide visual perception of the surrounding [5]. As shown in Fig. 1a3, there are ~100-120 millions of photoreceptors, rod and cone cells, vertically assembled in the retina in a dense and quasi-hexangular manner. The density of these photosensing cells is around 10 million/cm^2 with 3 μm average pitch, thus a human retina has a very high imaging resolution comparable with the state-of-the-art CCD/CMOS sensors[6]. However, the nerve fiber layer is at the front surface of human retina causing light loss and blind spot issues (Extended Data Fig. 1)[5]. Figure 1b1 and 1b2 illustrate the schematic of our biomimetic visual system, which has a very high degree of similarity to its natural counterpart consisting a lens, photosensor array on a hemispherical substrate and thin liquid metal (LM) wires as electrical contacts. These components mimic biological eye lens, retina and nerve fibers behind the retina, respectively. Among them,

the key component is the artificial retina made of a high-density array of NWs grown inside hemispherical porous-alumina-membrane (PAM) via a vapor-phase growth process[7-9].

A more detailed structure of the EC-EYE is in Fig. 2a, and the fabrication process is in Extended Data Fig. 2. The NWs serve as light-sensitive working electrodes. The Tungsten (W) film on Aluminum (Al) hemispherical shell works as the counter electrode. In between two electrodes, ionic liquid 1-Butyl-3-methylimidazolium bis(trifluoromethylsulfonyl)imide (BMIMTFSI) mixed with 1v% of 1-Butyl-3-methylimidazolium iodide (BMIMI) is used to fill in the spherical cavity serving as the electrolyte, mimicking the vitreous humour in a real human eye. There is also an aperture as the counterpart of a pupil in a human eye. The flexible Eutectic Gallium Indium (EGaIn) LM wires in soft rubber tubes are used for signal transmission between NWs and external circuitry. A Polydimethylsiloxane (PDMS) socket with pore arrays is used to assemble these tubes forming electrical contacts to NWs. The individual photodetector can be addressed and measured by selecting the corresponding LM wire. This resembles the working principle of human retina in which groups of photoreceptors, with up to thousands of receptors in one group[10], are individually connected with nerve fibers, enabling suppressed interference among pixels and high-speed parallel processing of the neuroelectric signals. Note that in our device, the LM wires are behind the sensing material, and thus unlike human retina, it does not have the aforementioned light loss and blind spot issue. In this work, as a concept-proof, 100 photodetectors were fabricated into a square 10×10 photodetector array with pitch of ~1600 μm. Each photodetector has a footprint of ~3.84×10^{-3} cm^2 (700 μm in diameter) containing ~1.5×10^6 NWs. Note that the minimum size of each sensing pixel is limited by the diameter of LM wire which is challenging to reduce to a few micrometers[11]. To further reduce sensor pixel size thus increasing

spatial imaging resolution, we have developed a parallel approach to fabricate sensor pixel array with each pixel area of ~1 μm^2 using metal microneedles which will be discussed later.

It is noteworthy that previously there have been a few inspiring works reporting hemispherical image sensors using deformed, folded or individually assembled photodetectors[12-14]. Photodetectors in those works were mainly pre-fabricated on planar substrates, then transferred to hemispherical supporting material or folded to hemispherical shape. It is challenging to achieve small individual pixel size and high imaging resolution due to the complexity of the fabrication process. However, here light sensing NWs are naturally grown in a hemispherical template thus a unique structure akin to human retina is formed in one step. Also, as NWs have density beyond that of photoreceptors on human retina, the NW retina has potency to deliver higher image resolution as mentioned above. Formamidinium lead iodide ($FAPbI_3$) was chosen as the model material for NWs growth here since it has excellent stability among organic-inorganic hybrid perovskites[15]. The NW growth and characterization details can be found in Methods section and Extended Data Fig. 3&4. In principle other types of inorganic NWs made of Si, Ge, GaAs, *etc*., can also be grown using the well documented vapor-liquid-solid process[16-19]. Figure 2b&c show the side- and top-view of completed EC-EYE. Figure 2d&e present the cross-sectional SEM images of hemispherical PAM and NWs located at bottom of the nanochanncels with length of ~5 μm, diameter of ~120 nm, and pitch of 500 nm corresponding to NW density of 4×10^8 cm^{-2}. This NW pitch is around 6 times smaller than the average pitch of photoreceptors in human retina, indicating a promising potency to achieve high imaging resolution if proper electrical contacts can be achieved[20]. Figure 2f presents the high resolution transmission-electron-microscopy (HRTEM) imageof one representative NW confirming the single crystallinity of grown NWs. And Figure 2g

shows the PDMS socket casted from a three-dimensional (3D) printed mode for LM wire assembly.

After device fabrication, performance of individual pixels has been systematically characterized before image sensing test. Figure 3a shows the configuration of a single pixel measurement. A beam of collimated light passing through the lens and electrolyte is focused on the pixels at the center of retina. Figure 3b plots the energy band alignment for the entire device showing charge carrier separation routes under light excitation. Figure 3c presents the current-voltage (*I*-*V*) characteristics of an individual pixel (back contact size ~ 700 μm) exhibiting asymmetric photo-response. The asymmetric nature of the *I*-*V* curves can be explained by the asymmetric charge transportation at the two sides of $FAPbI_3$ NWs (Figure 3b). More electrochemical characterizations have shown that the redox reactions of I^-/I_3^- pairs[21,22] occur at the NW/electrolyte and W film/electrolyte interfaces and ion transportation inside the electrolyte contribute to the observed photo-response with details in Extended Data Fig. 5. The inset of Figure 3c shows the transient response of the EC-EYE system to chopped halogen light under -3V bias with the result using lower bias shown in Extended Data Fig. 6. The relatively fast and highly repeatable response indicates that the device has excellent photocurrent stability and reproducibility. The detailed time response measurements can be found in Extended Data Fig. 7. And the response and recovery time are found to be 32.0 ms and 40.8 ms. Further electrochemical analysis of the critical NW/electrolyte interface revealed the device response time depends on the kinetics of multiple types of ions at that interface (Extended Data Fig. 8). More electrochemical-impedance-spectroscopy (EIS) measurements (Extended Data Fig. 9) demonstrate that by removing the subchannel layer part of NW at the bottom of the PAM and increasing BMIMI concentration to 10% can substantially reduce the charge-transfer-resistance (R_{ct}) at the

NW/electrolyte interface leading to significant reduction of device response and recovery time down to 19.2 ms and 23.9 ms, respectively. This response speed is already much faster than that of human photoreceptors ranging from 40 ms to 150 ms[23].

Human eyes can accommodate large change from dark to bright environment. Figure 3d shows the dependence of photocurrent and responsivity on the illumination intensity. The device shows a large dynamic range from 0.3 μWcm^{-2} to 50 $mWcm^{-2}$. The photocurrent can be fitted with a quasi-linear power law relationship ($I \sim P^{0.69}$), where I is the photocurrent and P represents the irradiance power. As mentioned above, the sensing NWs in our device are directly exposed to light, which can benefit device performance and lead to high responsivity and low detection limit. Intriguingly, the responsivity increases when reducing illumination intensity. It can reach up to 303.2 mAW^{-1}, which is among the highest in the reported photoelectrochemical (PEC) photodetectors (Extended Data Table 1) to our best knowledge. And it is in par with that of solid-state photodetectors based on perovskite NW arrays reported earlier[7,8]. Under the lowest radiation level measured, the number of photons received per second by an individual nanowire can be estimated as 23 photons (Extended Data). This sensitivity is already much better than that of a human cone cell, which has response to 100-1000 photons per second[24]. The corresponding specific detectivity is calculated as ~2.7×10^9 Jones to 0.3 μWcm^{-2} incident light. And the spectral responsivity was measured with light intensity of 10 $mWcm^{-2}$ (Extended Data Fig. 11), the device demonstrates a broad-band response with a clear cut-off at 810 nm, matching the band-gap of $FAPbI_3$ NWs (Extended Data Fig. 4b). Extended Data Fig.12 demonstrates the stability of and repeatability of an individual pixel under 2 Hz continuously chopped light for 9 hrs. It shows that although there are drifts for both dark and light currents, there is no obvious device performance degradation after 64,800 cycles.

As mentioned, one of the primary merits of using high-density NW arrays for artificial retina is their potency toward high imaging resolution. Though LM fiber contacts to NWs are convenient and image resolution is already in par with a number of existing bionic eyes in use[25-27], it is challenging to reduce pixel size down to single-digit-micrometer level. Thus two more contact strategies were developed to achieve ultra-small pixel size. As shown in Figure 3e, a single perovskite NW was deterministically grown in a single PAM nanochannels opened by focused ion beam (FIB) then a single pixel with 500 nm lateral size and footprint of ~0.22 μm^2 was achieved (Methods section and Extended Data Fig. 13). With the same approach, a pixel consists of 4 NWs was also fabricated. The SEM images in Extended Data Fig.14 show the controllable growth of NWs, including the NW numbers and positions, enabled by FIB. The photo-responses of these two devices are shown in Figure 3e. To form array of ultra-small pixels, Nickel (Ni) microneedles were vertically assembled on top of a PAM by magnetic field thus each microneedle can address 3 NWs forming a pixel with lateral size ~ 1μm and pitch of 200 μm. The detail of this contact strategy is illustrated in Extended Data Fig. 15&16. Figure 3f schematically shows the device connected to copper wires signal transmission lines. And the lateral size of the contact region is 2 mm.

After characterization of individual sensor pixels, the full device imaging functionality was measured. A photograph of the device is shown in Fig. 4a and Extended Data Fig. 17a&b. The LM wires are connected to a computer controlled 100×1 multiplexer via a printed-circuit-board (PCB). The measurement system design is in Fig. 4b and the corresponding circuit diagram is demonstrated in Extended Data Fig. 17c. The image sensing function was examined by projecting optical patterns onto the EC-EYE then photocurrent of each sensor pixel was recorded. Before pattern generation and recognition, it is important to verify the consistency of the dark and light current of all pixels. Extended Data Fig. 18a&b demonstrate the dark and light current images

obtained under -3 V bias voltage, showing all 100 pixels have descent photoresponse with relatively small variation. To reconstruct the optical pattern projected on the EC-EYE, a photocurrent value was converted to grayscale number between 0 and 255 (Extended Data). Figure 4c demonstrates the imaged character "A" and its projection on a flat plane. Extended Data Fig. 19 shows images of "E", "I" and "Y". Supplementary Movie 1 shows the dynamic process of EC-EYE capturing letters of "E", "Y" and "E" sequentially. Compared to planar image sensors based on crossbar structure, the device here delivers higher contrast with clearer edges since each individual pixels are better isolated from the neighboring pixels (Extended Data Fig. 20)[7]. Besides an EC-EYE with LM contacts, a small EC image sensor with microneedle contacts was also fabricated as mentioned above. The imager with an active area of 2 mm × 2 mm was assembled into a mini-camera together with other optical parts (Extended Data Figure 21&22). Extended Data Figure 22 shows its imaging functionality. Meanwhile, the developed magnetic microneedle alignment strategy works also very well for the whole hemispherical surface. Extended Data Fig. 23 shows that the 50 μm-thick Ni microwires are well aligned onto the surface of a hemispherical PAM.

The successful pattern imaging with our devices has proved their potential for future high-performance visual system approaching or beyond natural human eyes. Compared to a planar image sensor, the hemispherical shape ensures a more consistent distance between pixels and lens, resulting in a wider FOV and better focusing on all pixels, as illustrated in Fig. 4d1. The diagonal visual field of our hemispherical EC-EYE is estimated as ~100.1^{o} while that of planar device is only 69.8^{o}, as plotted in Fig. 4d2. This has clearly demonstrated the improvement in FOV of our hemispherical device compared to its planar counterpart. Moreover, this angle of view can be further improved to approach the static FOV of a single human eye, which is ~130^{o} without

considering the eye/head movement[28], by optimizing the pixel distribution and the shape of PAM beyond hemisphere.

Here we have demonstrated a biomimetic artificial eye with a hemispherical retina made of high-density light-sensitive NWs. It has a structure with high degree of similarity to that of a natural human eye while with a potency to achieve higher imaging resolution if proper contact strategy can be implemented. The developed processes can tackle the bottleneck challenge on fabricating optoelectronic devices on non-planar substrates with high integration density. Furthermore, our exploration here can also inspire novel designs of new generation optical imaging devices based on biomimetics that can benefit a wide spectrum of technological applications in scientific instrumentation, consumer electronics, robotics, *etc*.

Online content

Any methods, additional references, Nature Research reporting summaries, source data, statements of data availability and associated accession codes are available at XXX.

Received: XX; Accepted: XX; Published online XX.

References:

1. Pocock, D. C. D., Sight and knowledge. *Trans. Inst. Br. Geogr*., 385-393 (1981).
2. Lee, G. J., Choi, C., Kim, D. H. & Song, Y. M. Bioinspired artificial eyes: Optic components, digital cameras, and visual prostheses. *Adv. Funct. Mater.* **28**, 1705202 (2017).
3. Jung, I. et al. Dynamically tunable hemispherical electronic eye camera system with adjustable zoom capability. *Proc. Natl. Acad. Sci.* **108**, 1788-1793 (2011).
4. Nassi, J. J. & Callaway, E. M. Parallel processing strategies of the primate visual system. *Nat. Rev. Neurosci.* **10**, 360-372 (2009).

5. Atchison, D. A. & Smith, G. *Optics of the human eye (Vol. 35).* (Oxford: Butterworth-Heinemann, 2000).
6. Jonas, J. B., Schneider, U. & Naumann, G. O. Count and density of human retinal photoreceptors. *Graefes Arch. Clin. Exp. Ophthalmol.* **230**, 505-510 (1992).
7. Gu, L. et al. 3D Arrays of 1024-Pixel Image Sensors based on Lead Halide Perovskite Nanowires. *Adv. Mater.* **28**, 9713-9721 (2016).
8. Gu, L. et al. Significantly improved black phase stability of $FAPbI_3$ nanowires via spatially confined vapor phase growth in nanoporous templates. *Nanoscale* **10**, 15164-15172 (2018).
9. Waleed, A. et al. Lead-free perovskite nanowire array photodetectors with drastically improved stability in nanoengineering templates. *Nano Lett.* **17**, 523-530 (2017).
10. Schein, S. J., Anatomy of macaque fovea and spatial densities of neurons in foveal representation. *J. Comp. Neurol.* **269**, 479-505 (1988).
11. Dickey, M. D. et al. Eutectic gallium-indium (EGaIn): a liquid metal alloy for the formation of stable structures in microchannels at room temperature. *Adv. Funct. Mater.* **18**, 1097-1104 (2008).
12. Song, Y. M. et al. Digital cameras with designs inspired by the arthropod eye. *Nature* **497**, 95-99 (2013).
13. Ko, H. C., Stoykovich, M. P., Song, J., Malyarchuk, V., Rogers, J. A. A hemispherical electronic eye camera based on compressible silicon optoelectronics. *Nature* **454**, 748-753 (2008).
14. Zhang, K. et al. Origami silicon optoelectronics for hemispherical electronic eye systems. *Nat. Commun.*, 8, 1-8 (2017).

15. Han, Q. et al. Single crystal formamidinium lead iodide ($FAPbI_3$): Insight into the structural, optical, and electrical properties. *Adv. Mater*. **28**, 2253-2258 (2016).
16. Fan, Z. et al. Ordered arrays of dual-diameter nanopillars for maximized optical absorption. *Nano Lett*. **10**, 3823-3827 (2010).
17. Fan, Z. et al. Three-dimensional nanopillar-array photovoltaics on low-cost and flexible substrates. *Nat. Mater*. **8**, 648-653 (2009).
18. Ramdani, M. R. et al. Fast growth synthesis of GaAs nanowires with exceptional length. *Nano Lett*. **10**, 1836-1841 (2010).
19. Wen, C. Y. et al. Formation of compositionally abrupt axial heterojunctions in silicon-germanium nanowires. *Science* **326**, 1247-1250 (2009).
20. Wandell, B. A., Foundations of vision (Sunderland, MA: Sinauer Associates, 1995), Vol. 8.
21. Boschloo, G. & Hagfeldt, A. Characteristics of the iodide/triiodide redox mediator in dye-sensitized solar cells. *Acc. Chem. Res*. **42**, 1819-1826 (2009).
22. Kawano, R. & Watanabe, M., Equilibrium potentials and charge transport of an I^-/I_3^- redox couple in an ionic liquid. *Chem. Comm.* **3**, 330-331 (2003).
23. Rayner, K., Smith, T. J., Malcolm, G. L. & Henderson, J. M. Eye movements and visual encoding during scene perception. *Psychol. Sci*. **20**, 6-10 (2009).
24. Mustafi, D., Engel, A. H. & Palczewski, K. Structure of cone photoreceptors. *Prog. Retin. Eye Res.* **28**, 289-302 (2009).
25. Fujikado, T. et al. Evaluation of phosphenes elicited by extraocular stimulation in normals and by suprachoroidal-transretinal stimulation in patients with retinitis pigmentosa. *Graefes Arch. Clin. Exp. Ophthalmol.* **245**, 1411-1419 (2007).

26. Ayton, L. N. et al. First-in-human trial of a novel suprachoroidal retinal prosthesis. *PloS one* **9**, e115239 (2014).
27. Shivdasani, M. N. et al. Factors affecting perceptual thresholds in a suprachoroidal retinal prosthesis. *Invest. Ophth. Vis. Sci.* **55**, 6467-6481 (2014).
28. Navarro, R., The optical design of the human eye: a critical review. *J. Optom*. **2**, 3-18 (2009).

Acknowledgments This work was supported by the National Natural Science Foundation of China (project 51672231) and Science & Technology Plan of Shenzhen (JCYJ20170818114107730), General Research Fund (Projects 16237816, 16309018) from the Hong Kong Research Grant Council and Hong Kong Innovation Technology Commission (project ITS/115/18). The authors acknowledge the support received from the Material Characterization & Preparation Facility (MCPF), Center for 1D/2D Quantum Materials and State Key Laboratory on Advanced Displays and Optoelectronics at HKUST. L. G. and Z. F. acknowledge discussions with Dr. Qing Chen and Dr. Minhua Shao at HKUST on electrochemistry.

Reviewer information *Nature* thanks XX and the other anonymous reviewer(s) for their contribution to the peer review of this work.

Author contributions Z. F. and L. G. conceived the ideas of the work; L. G., S. P., Z. L., D. Z, Q. Z., X. Q. and M. K. fabricated the device and performed the image sensing characterization. Y. L developed the photoelectrochemical working mechanism. L. G, Y. L., A. J. and Z. F. carried out the data analysis and wrote the manuscript. All authors discussed the results and commented on the manuscript. Authors declare no competing interests. All data is available in the main text or the Extended Data.

Competing interests The authors declare no competing interests.

Additional information

Extended data is available for this paper at XXX.

Reprints and permissions information is available at http://www.nature.com/ reprints.

Correspondence and requests for materials should be addressed to Z. Fan.

Publisher's note: Springer Nature remains neutral with regard to jurisdictional claims in published maps and institutional affiliations.

Methods

Fabrication of EC-EYE. The spherical EC-EYE fabrication starts with the creation of hemispherical Al shells which is fabricated by deforming a thick Al sheet by a set of hemispherical modes. The hemispherical Al shells underwent a standard two-step anodization process to form PAM on the surface. A barrier thinning process and Pb electrodeposition were carried out to obtain Pb nanoclusters at the bottom of PAM channels. Afterwards, the outer layer of PAM and the residual Al were etched away to obtain freestanding PAM with Pb, which was then transferred into a tubular furnace for NW growth. An Indium layer was evaporated onto the PAM back surface to serve as adhesion layer. To obtain contact array, a hedgehog shaped mode was fabricated through 3D printing, from which a complementary PDMS socket was casted. EGaIn liquid metal was then injected into thin soft tubes to form liquid metal wires. These tubes were then inserted into the holes on PDMS socket and the whole socket was attached to the PAM/NW surface to form the contact arrays. Note that these Indium layer will not cause shortage between pixels due to its discontinuous morphology (Extended Data Fig. 24). 100 tubes were inserted to form a square 10×10 photodetector array. These long soft tubes can be directly connected to printed circuit board (PCB) and thus the complex wire bonding process is avoided. A circular hole was opened on

another Al shell, which was then coated with a tungsten film working as counter electrode of EC-EYE. The Al shell was subsequently fixed onto front side of PAM by epoxy. Ionic liquid mixture is then injected and a lens was then glued to the hole on Al shell to seal the device. After curing, the EC-EYE device fabrication was completed.

Fabrication of microneedles based electrochemical image sensor. Freestanding PAM of 50 μm thick was fabricated by standard anodization process, NaOH etching and $HgCl_2$ solution etching. Ion milling is used to remove the barrier layer to achieve through-hole PAM (Extended Data Fig. 16a). Then Cu film of 1 μm thick was thermally evaporated to onto the through-hole PAM to serve as the electrode for the subsequent Ni and Pb electrochemical deposition (Extended Data Fig. 16b). Afterwards, to expose the Ni NWs, the copper layer is removed by ion milling and the PAM was partially etched away by Reactive Ion Etching (RIE). The exposed Ni nanowires was about 3 μm long (Extended Data Fig. 16c). The chip is moved into tubular furnace for perovskite NW growth (Extended Data Fig. 16c). The PAM chip is fixed on an electromagnet with Ni nanowires facing upward (Extended Data Fig. 16d). Meanwhile, Ni microwires of 50 μm diameter were sharpened in a mixed acidic solution (100 ml 0.25M HCl aqueous solution+100 ml EG) under the bias of 1 V, with Ni microwires as working electrodes and tungsten coil as counter electrode. The resulted Ni microwires have sharp tips, with curvature radius ranging from 100-200 nm. The Ni needle is then gently landed onto the PAM substrate with the magnetic field ON. Due to the magnetic force, the ferromagnetic Ni microneedles can engage into the Ni NW forest to from effective electrical contact to NWs (Extended Data Fig. 16d). To facilitate Ni microwire landing, a mask with 10×10 hole array (hole diameter: 100 μm, pitch: 200 μm) was used to align the Ni microneedles (Extended Data Fig. 16d). After landing, UV epoxy was dropped between the mask and PAM substrate. Copper enameled wire with diameter of 60 μm was inserted into the hole to form

electrical contact bridging the Ni microneedle and external PCB board (Extended Data Fig. 16e).

Fabrication of single and multiple NW based EC photodetector. Freestanding planar PAM was fabricated by standard two-step anodization followed by $HgCl_2$ etching. The freestanding PAM was then transferred into FIB (FEI Helios G4 UX) to selectively etch away the barrier layer (Extended Data Fig. 13c). To facilitate the etching, the chip was bonded on an Al substrate with barrier layer side facing up. After FIB etching (etching voltage: 30kV, etching current: 26 nA), a 500 nm-thick Cu layer was evaporated onto the barrier layer side to serve as the electrode for the subsequent Pb electrochemical deposition (Extended Data Fig. 13d). Afterward, the chip was moved into a tubular furnace for perovskite NW growth (Extended Data Fig. 13e). Then a copper wire was bonded onto the Cu side of PAM by carbon paste and the whole chip is fixed onto a glass substrate by UV epoxy. After curing, ionic liquid was dropped onto the top of PAM (Extended Data Fig. 13e). And a Tungsten probe was inserted in the ionic liquid for photoelectric measurement.

Material and photodetector characterization. The SEM images and Energy Dispersive X-ray (EDX) mapping of PAM were characterized using a field-emission scanning electron microscopy (JEOL JSM-7100F equipped with a Si (Li) detector and PGT 4000T analyzer. XRD patterns of $FAPbI_3$ NW arrays in PAM were obtained using Bruker D8 X-ray diffractometer. TEM images were obtained by TEM JEOL (2010) with 200 kV acceleration voltage. UV-vis absorption was measured by Varian Cary 500 spectrometer (Varian, USA). The PL and TRPL measurements were carried out on Edinburgh FS5 fluorescence spectrometer. The EIS measurements were performed in a bi-electrode mode in an electrochemical workstation, i.e. Gamry Instruments, USA. The frequency range used was 300 kHz to 100 Hz at a biasing voltage of -3 V. *C-V* measurements based on a two-electrode configuration were performed on an electrochemical workstation (CHI

660E, China) at a scan rate of 100 mVs^{-1} with solar simulated AM 1.5 as the light source. The *I-t* curves of individual pixel were measured by probe station of HP4156A with ND filters to tune the light intensity. An additional chopper was inserted to chop light into alternative signals with different frequency. The Electrochemical Impedance Spectra (EIS) were measured by potential state Gamry SG 300 in a range of 300 KHz-100 Hz, with amplitude of 10 mV under the bias of -3V. The working electrodes connecting to the liquid metal. The reference and counter electrode are connected with the Tungsten electrode.

Image sensing characterization of EC-EYE. The image sensing performance of EC-EYE was characterized by using a home-built system consisting of a multiplexer, a pre-amplifier, a laptop computer and a labview program. The schematic of the system can be found in Fig. 4b. Specifically, Keithley 2400 was used to provide the bias voltage. The current meter (PXI4130, National Instruments), together with multiplexer (PXI2530B, National Instruments), was installed inside of a chasis (PXI1031, National Instruments). The whole system is controlled by a home-built Labview computer program. To carry out the measurements, various optical patterns were generated by PowerPoint slides and projected onto the device by a projector. A convex lens was used to focus the pattern and different Neutral Density filters were inserted between the projector and image sensor to tune the light intensity.

Data availability

The data that support the findings of this study are available from the corresponding author upon reasonable request.

References for Extended Data:

29. Xie, Y. et al. A self-powered UV photodetector based on TiO_2 nanorod arrays. *Nanoscale Res.*

Lett. **8**, 188 (2013).

30. Lin, H. et al. High-performance self-powered photodetectors based on ZnO/ZnS core-shell nanorod arrays. *Nanoscale Res. Lett.* **11**, 420 (2016).
31. Zeng, Y., Pan, X., Dai, W., Chen, Y. & Ye, Z. The enhancement of a self-powered UV photodetector based on vertically aligned Ag-modified ZnO nanowires. *RSC Adv.* **5**, 66738-66741 (2015).
32. Kim, C. W., Suh, S. P., Choi, M. J., Kang, Y. S. & Kang, Y. S. Fabrication of $SrTiO_3$-TiO_2 heterojunction photoanode with enlarged pore diameter for dye-sensitized solar cells. *J. Mater. Chem. A* **1**, 11820 -11827 (2013).
33. Li, Z. et al. High‐Performance Photo‐Electrochemical Photodetector Based on Liquid-Exfoliated Few-Layered InSe Nanosheets with Enhanced Stability. *Adv. Funct. Mater.* **28**, 1705237 (2018).
34. Ren, X. et al. Zhang, Environmentally Robust Black Phosphorus Nanosheets in Solution: Application for Self‐Powered Photodetector. *Adv. Funct. Mater.* **27**, 1606834 (2017).
35. Li, J. et al. A high performance ZnO based photoelectrochemical cell type UV photodetector with $[Co(bpy)_3]^{3+/2+}$ electrolyte and PEDOT/ITO counter electrode. *RSC Adv.* **7**, 18987-18992 (2017).
36. Lin, P. et al., A tunable ZnO/electrolyte heterojunction for a self-powered photodetector. *Phys. Chem. Chem. Phys.***16**, 26697 -26700 (2014).
37. Patel, D. B., Chauhan, K. R. & Mukhopadhyay, I. Unraveling the photoelectrochemical properties of ionic liquids: cognizance of partially reversible redox activity. *Phys. Chem. Chem. Phys.***16**, 22735-22744 (2014).
38. Li, X. et al., High‐Performance Photoelectrochemical-Type Self-Powered UV Photodetector

Using Epitaxial TiO_2/SnO_2 Branched Heterojunction Nanostructure. *Small* **9**, 2005-2011 (2013).

39. Hou, X. et al. $SnO_2@TiO_2$ Heterojunction Nanostructures for Lithium-Ion Batteries and Self-Powered UV Photodetectors with Improved Performances. *Chem. Electro. Chem.* **1**, 108-115 (2014).
40. Wang, Z., Ran, S., Liu, B., Chen, D. and Shen, G. Multilayer TiO_2 nanorod cloth/nanorod array electrode for dye-sensitized solar cells and self-powered UV detectors. *Nanoscale* **4**, 3350-3358 (2012).
41. Yu, X., Prévot, M. S., Guijarro, N. & Sivula, K. Self-assembled 2D WSe_2 thin films for photoelectrochemical hydrogen production. *Nat. Commun.* **6**, 7596 (2015).

Figures

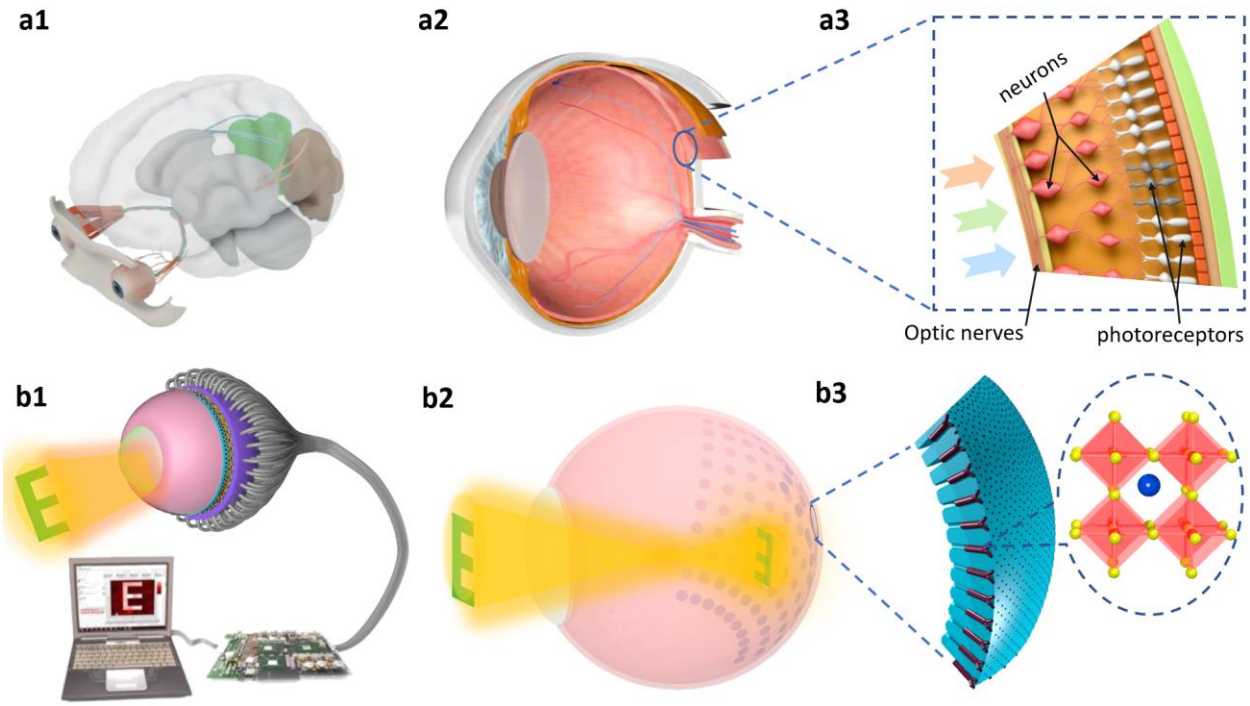

Fig. 1 | The overall comparison of the human and EC-EYE imaging systems. (**a1**) Schematic of human visual system, (**a2**) human eye and (**a3**) retina. (**b1**) Schematic of our EC-EYE imaging system, (**b2**) the working mechanism of our EC-EYE and (**b3**) NWs in PAM template and their molecular structure.

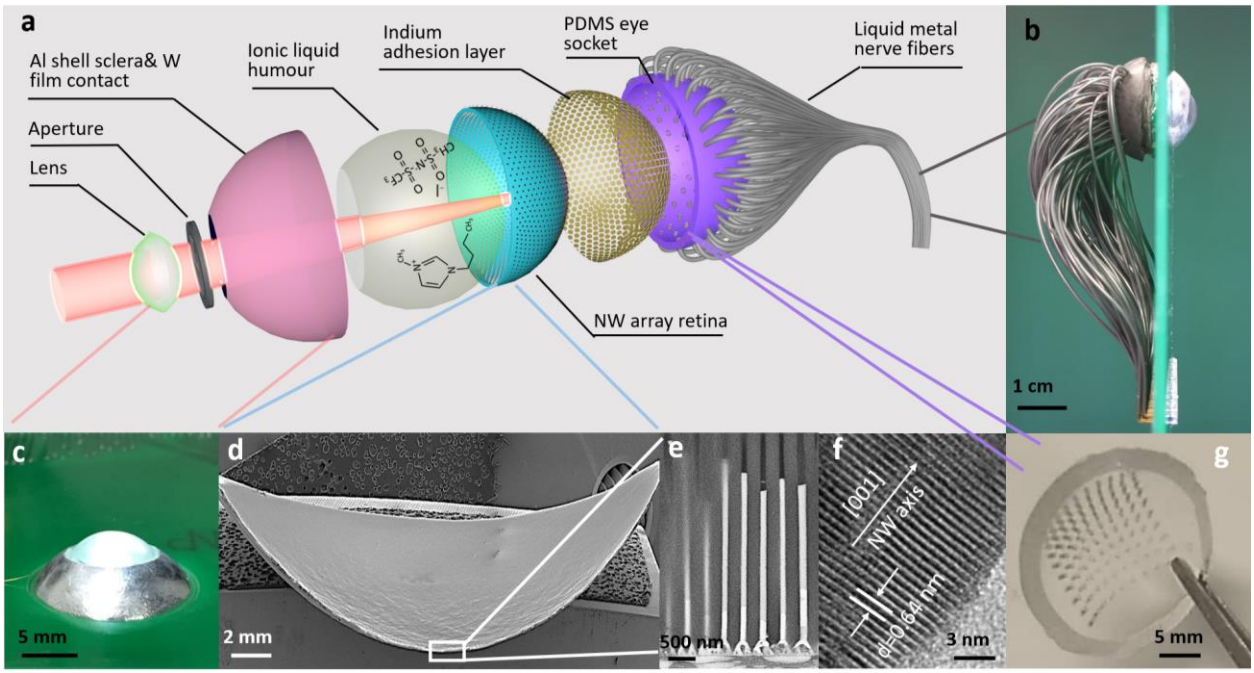

Fig. 2 | Detailed structure of our EC-EYE. (**a**) Layered structure of EC-EYE. (**b**) Side-view and (**c**) top-view of a completed EC-EYE. (**d**) Low resolution cross-sectional SEM image of hemispherical PAM/NWs. (**e**) Cross-sectional SEM images of NWs in PAM. (**f**) Representative HRTEM image of obtained individual NW. (**g**) Photo of PDMS socket to assist the alignment of liquid metal wires.

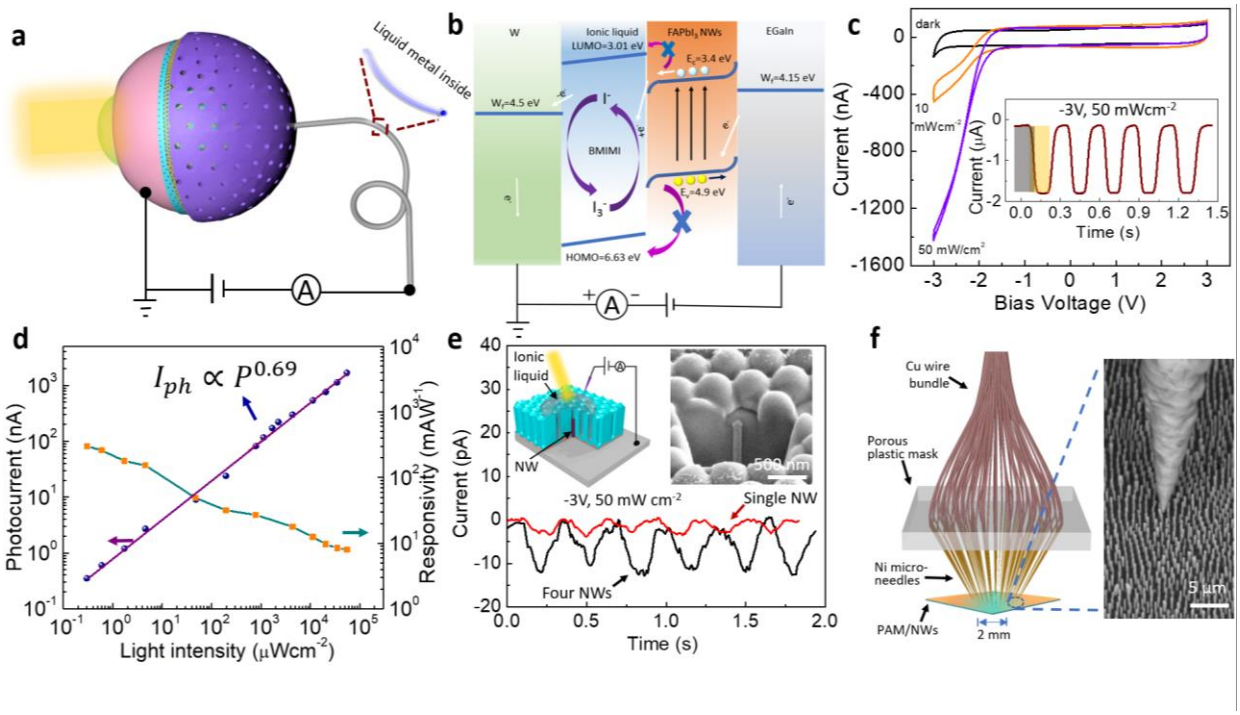

Fig. 3 | Photodetection performance characterization of individual pixel. (**a**) Schematic setup of individual pixel measurement. (**b**) Working mechanism of individual pixel under -3 V bias voltage. (**c**) Current-Voltage (*I-V*) curves under different illumination and transient response of individual pixel under the illumination of halogen light with intensity of 50 mWcm^{-2}. The *I-V* curves are in fact one cycle of cyclic voltammetry (*C-V*) measurement. Scan rate: 100 mV/s. (**d**) Illuminated intensity dependent photocurrent & responsivity of individual pixel. The lowest light intensity is 0.3 μWcm^{-2}. (**e**) Device schematic and transient photoresponse of single and four NWs based individual pixel. (**f**) The schematic and SEM image of Ni microneedle contact.

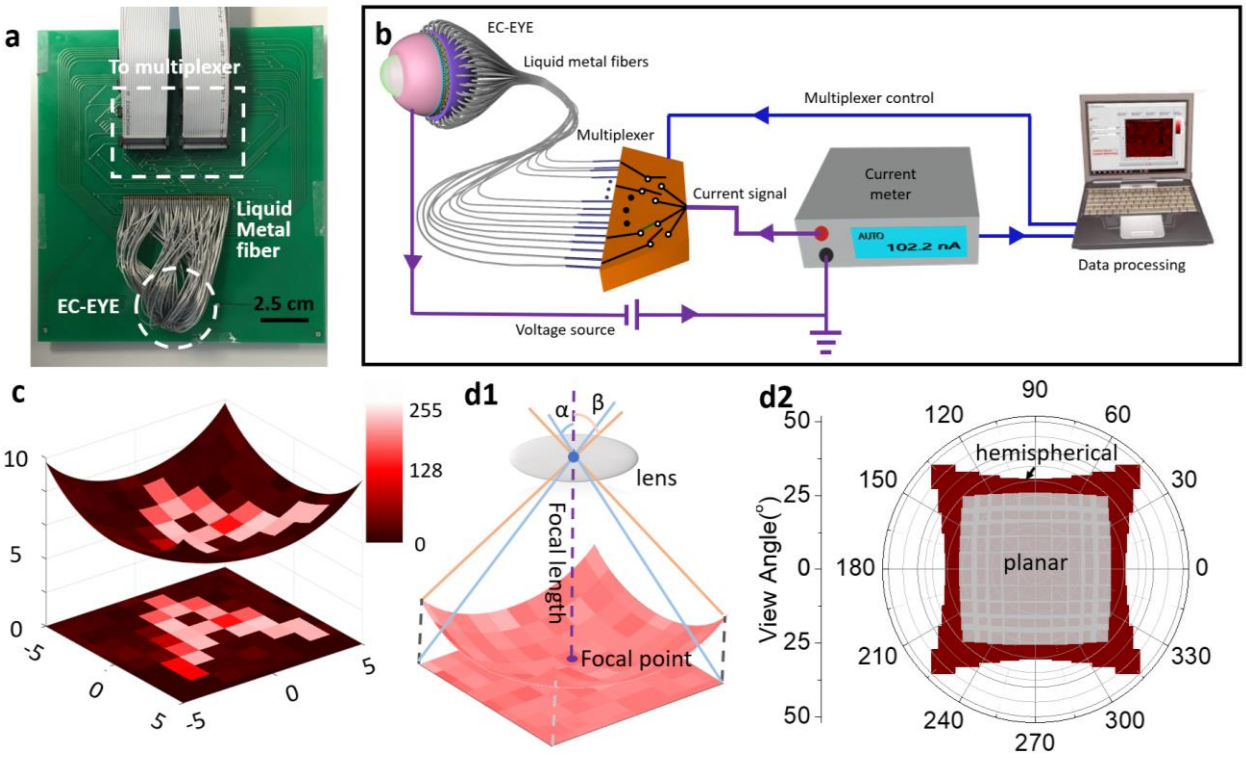

Fig. 4 | Image sensing performance characterization of EC-EYE. (**a**) The back of an EC-EYE mounted on PCB. (**b**) Schematic illustration of the measurement setup. (**c**) The reconstructed image (Letter "A") of EC-EYE and its projection on flat plane. (**d1**) The schematic and (**d2**) calculated FOV of planar and hemispherical image sensing systems.

Extended Data

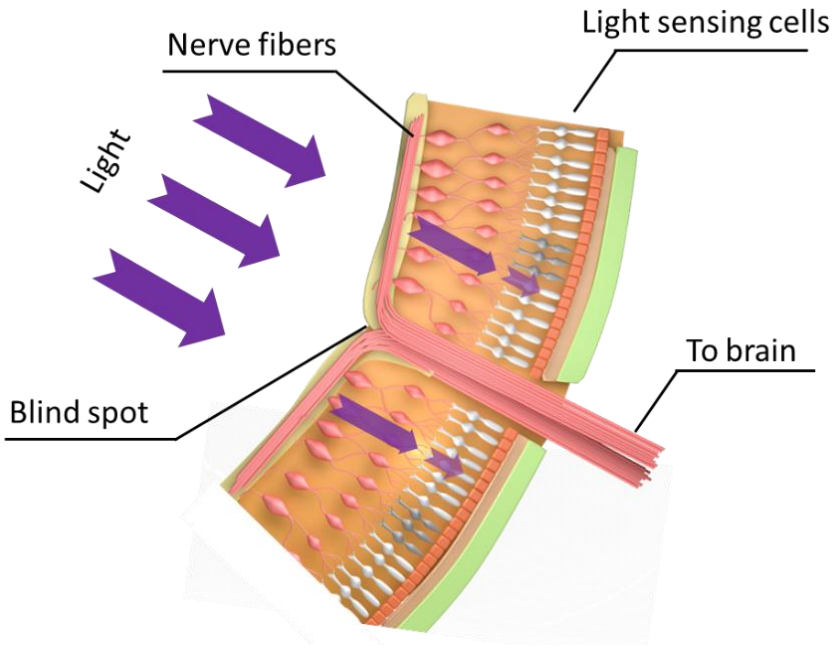

Extended Data Fig. 1 | Detailed structure of human eye retina. There is light loss through the optic nerve layers. As the nerve fibers route in front of the retina, there is a via where the fibers pass through the retina. This via is a blind spot on retina where there is no any photoreceptor.

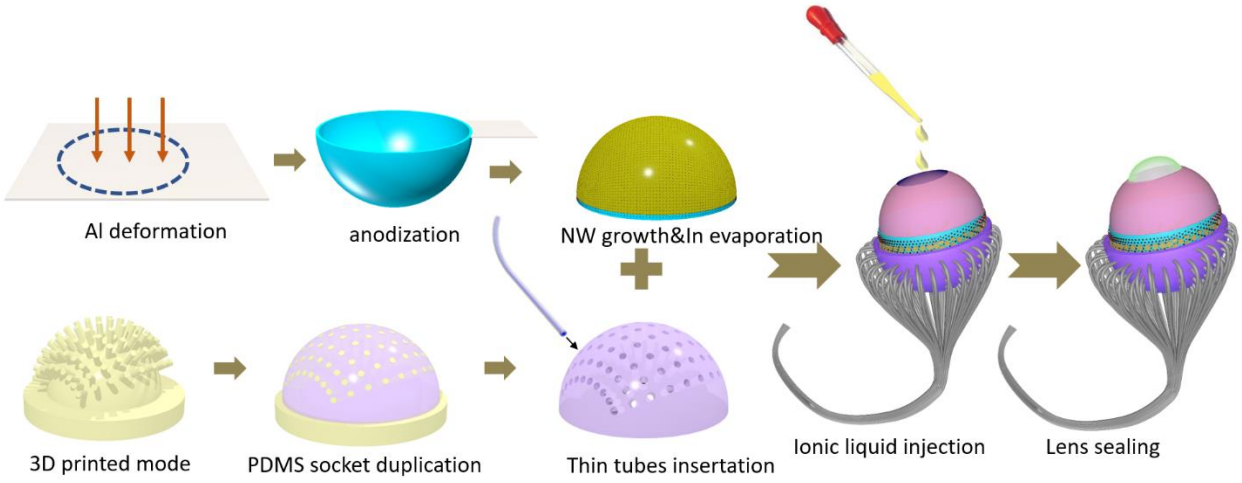

Extended Data Fig. 2 | The overall fabrication process of an EC-EYE. The process is a complex process combining new techniques such as 3D printing and liquid metal patterning.

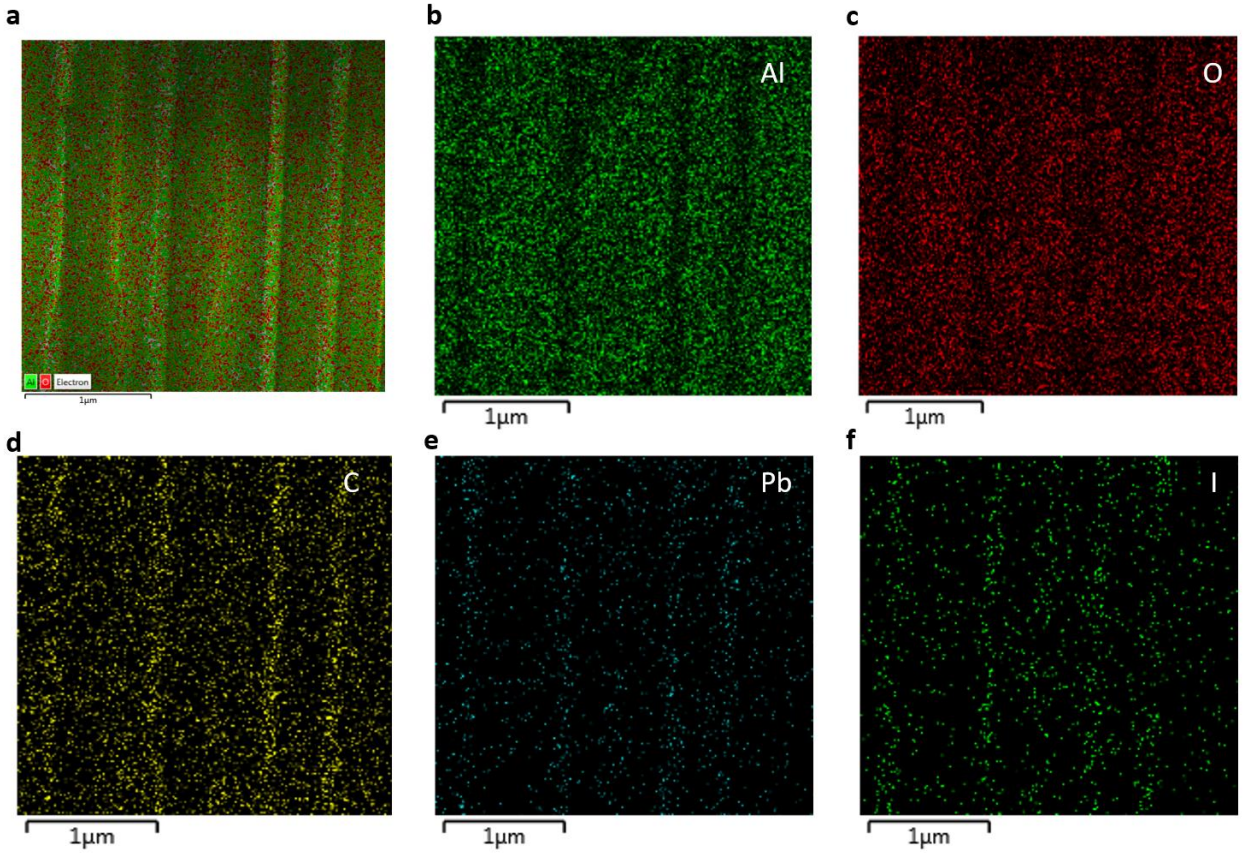

Extended Data Fig. 3 | Elemental analysis of $FAPbI_3$ NWs embedded in PAM. (**a**) Combined elemental mapping with signal from Al, O, C, Pb and I. (**b**), (**c**), (**d**), (**e**), and (**f**) are Al, O, C, Pb and I individual elemental mapping of the same NWs embedded in PAM.

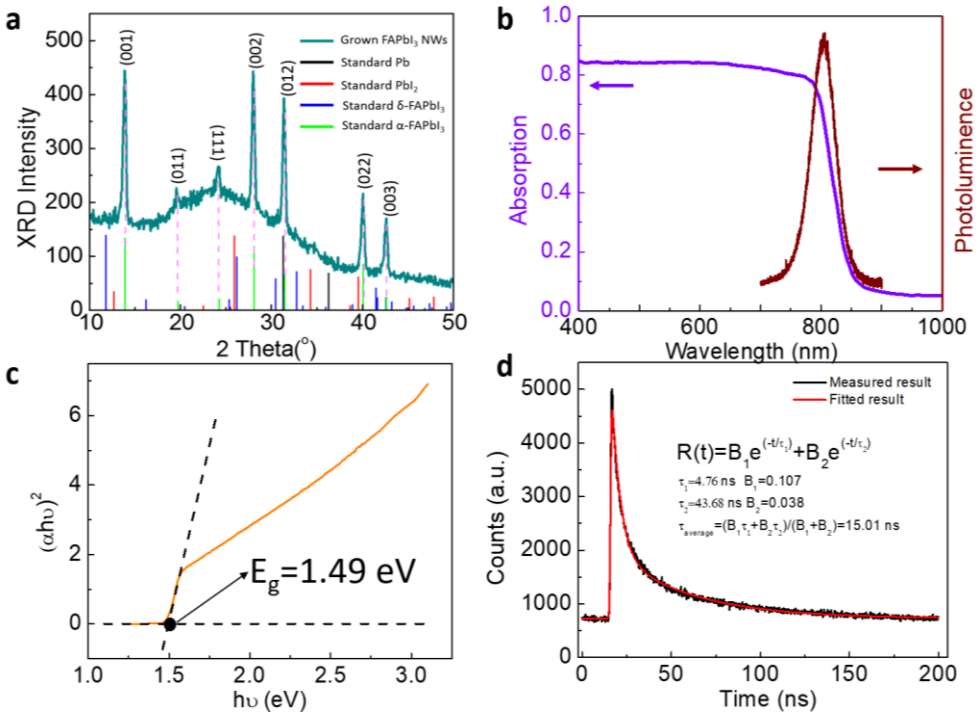

Extended Data Fig. 4 | Material characterization of perovskite NWs in PAM. (**a**) XRD pattern, (**b**) The photoluminescence and UV-vis spectra. (**c**) The Tauc plotting and (**d**) The time resolved photoluminescence of grown $FAPbI_3$ NWs in PAM.

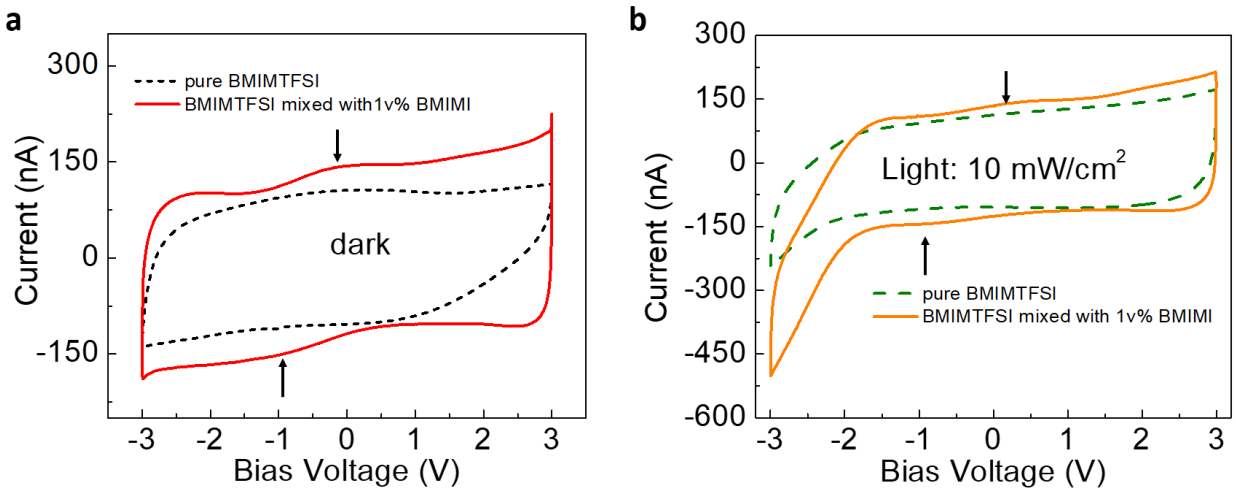

Extended Data Fig. 5 | Ionic liquid exploration. *C-V* curves of photodetectors based on pure and 1v% BMIMI mixed BMIMTFSI under dark (**a**) and light (**b**) conditions (illumination with 10 $mWcm^{-2}$, solar simulator light).

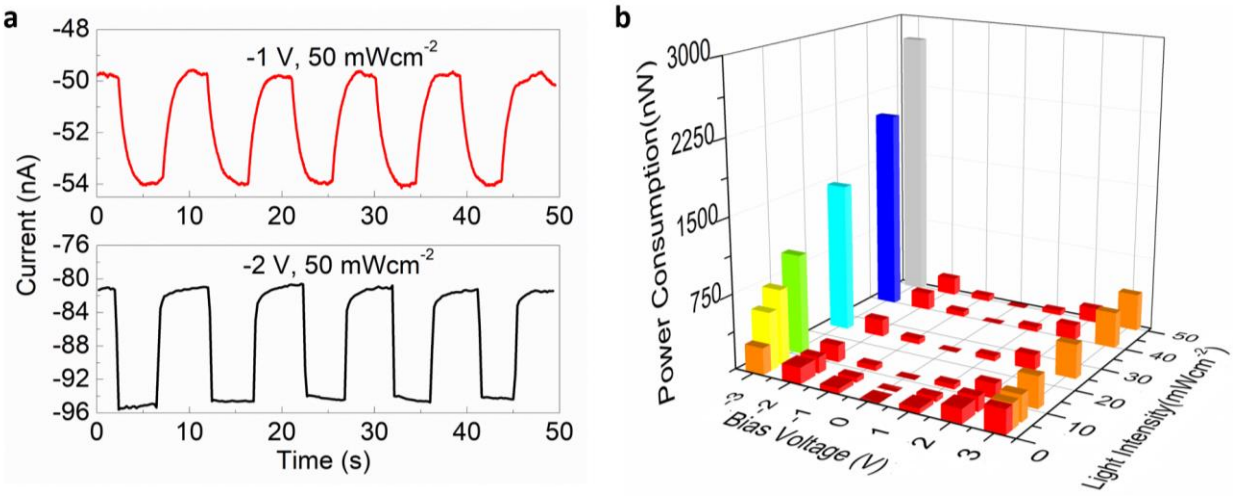

Extended Data Fig. 6 | (**a**)The *I-t* curves of individual pixel under lower bias voltage. (**b**) The power consumption of individual pixel under different bias and illumination conditions.

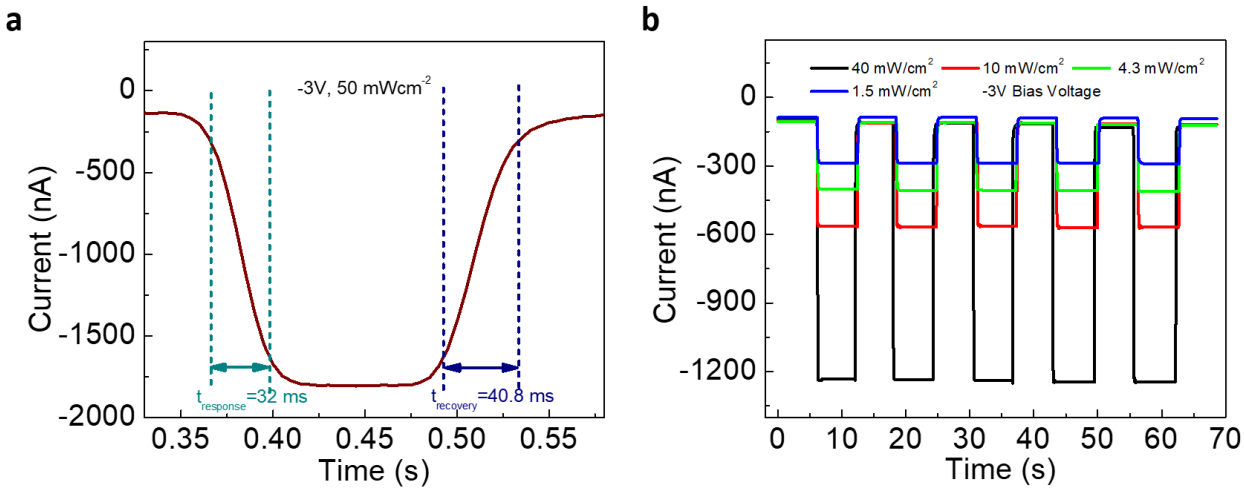

Extended Data Fig. 7 | (**a**) Photoresponse speed analysis of individual pixel. The light source is halogen light with intensity of 50 $mWcm^{-2}$. (**b**)Transient measurement of individual pixel to white light of different incident power.

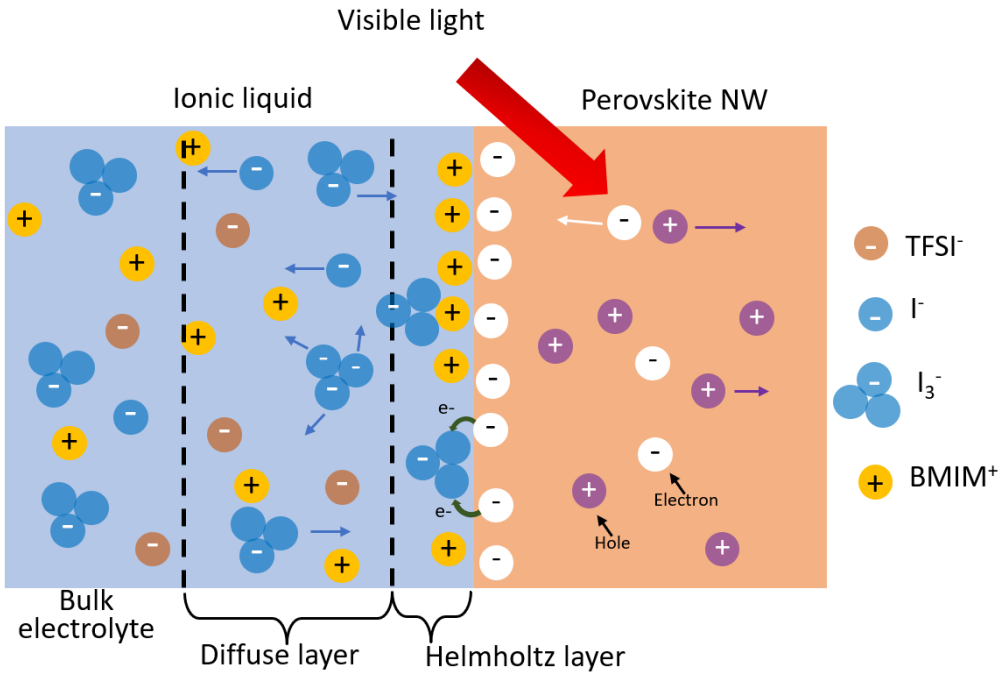

$$I_3^- + 2e^- \rightarrow 3I^-$$

Extended Data Fig. 8 | Ion and charge kinetics at NW/electrolyte interface. An electrical double layer is formed at the interface. The Helmholtz layer consists $BMIM^+$ ions adsorbed on perovskite surface and triiodide (I_3^-) ion in proximity. When light shines on perovskite NW and generates electron-hole pairs, photo-electrons move toward NW/electrolyte interface, leading to reduction of I_3^- to I^- and desorption of I^- followed by its diffusion toward W electrode.

Improving response speed of EC photodetectors

To improve response speed of our devices, we have explored two strategies to reduce R_{ct}. Firstly we have optimized our device by removing the subchannel layer between NWs and metal electrodes. The barrier thinning process prior to NW growth has led to formation of fine subchannels at the bottom of a PAM. NWs grown in this layer have small diameter and higher resistance than the NWs in the main channels, as shown in Extended Data Fig. 9a. EIS measurement (Extended Data Fig. 9b) shows R_{ct} of this device is 5.56 and 1.89 Mega ohm under dark and light (50 mW cm^{-2}). And the device response time and recovery time are 32 and 40.8 ms (Extended Data Fig. 9c). A mild ion milling process is used to remove the subchannel layer to facilitate carrier transport in NWs. Extended Data Fig. 9d shows the revised devices structure without the subchannel layer and Extended Data Fig. 9e shows the EIS measurement of the device. As suggested, the R_{ct} has significantly dropped to 1.31 and 0.92 Mega ohm for dark and light condition, indicating the accelerated charge transfer process. As the result, the device response and recovery speeds ($t_{response}$= 21.8 ms, $t_{recovery}$= 29.9 ms) has been improved.

In addition, increase concentration of I^-/I_3^- redox couple can further promotes charge transfer rate. Thus we have increased the BMIMI concentration from 1v % to 10 v%. Extended Data Fig. 9g shows the device structure. The EIS measurement result (Extended Data Fig. 9h) shows that the R_{ct} has been further reduced to 1.28 and 0.4 Mega ohm under dark and light conditions, respectively. Therefore, the response and recovery times have been reduced to 19.2 ms and 23.9 ms. Note that BMIMI has a broadband visible light absorbance (Extended Data Fig. 10). Thus BMIMI contraction cannot be too high to reduce the light loss before arriving at the NWs.

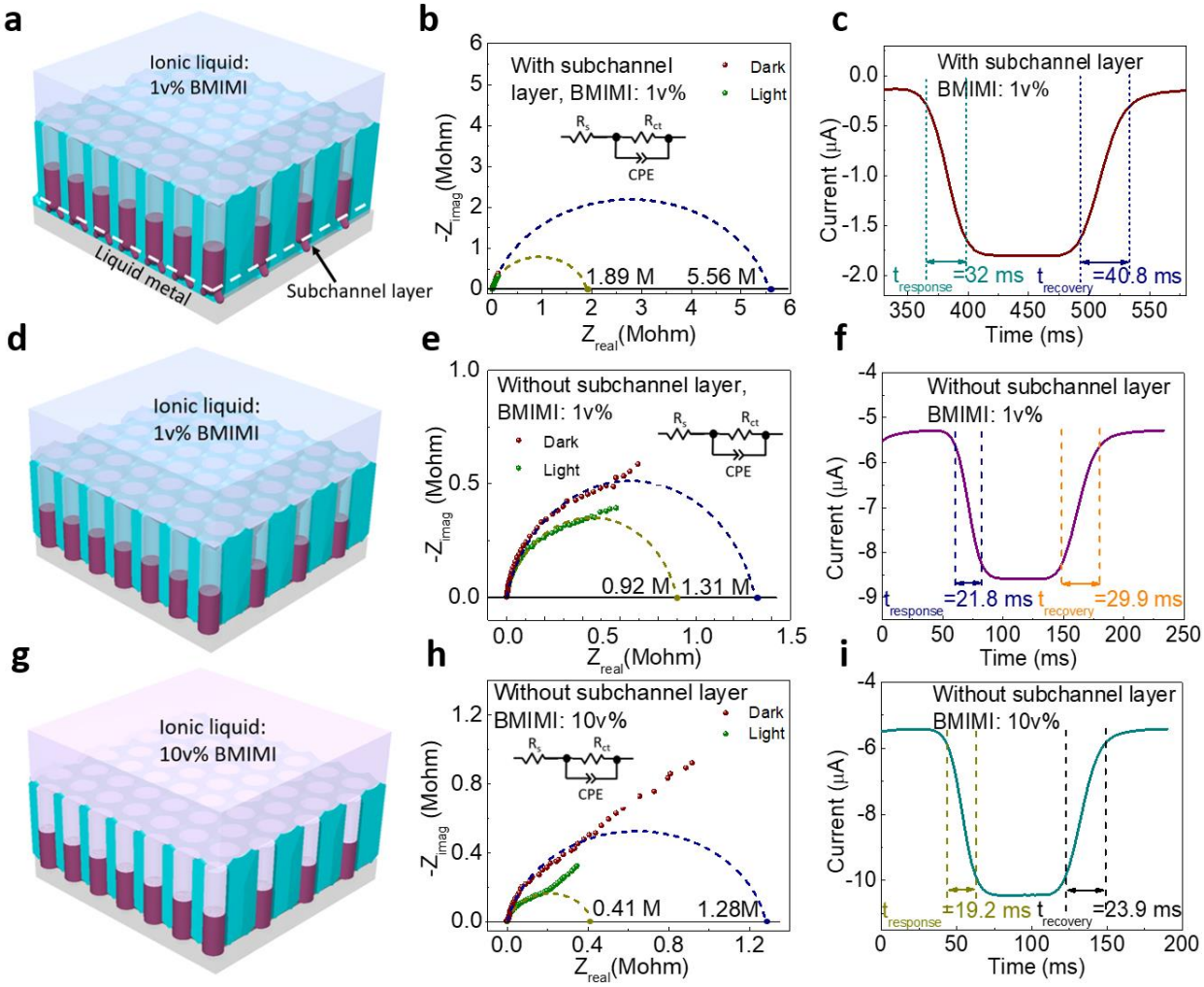

Extended Data Fig. 9 | (**a**) Schematic of a device with subchannel layer in ionic liquid with 1% BMIMI. (**b**) EIS measurement shows charge-transfer-resistance (R_{ct}) under dark and light and (**c**) shows device response time and recovery time are 32 ms and 40.8 ms, respectively. (**d**) Schematic of a device without subchannel layer in ionic liquid with 1% BMIMI. (**e**) EIS measurement shows charge-transfer-resistance (R_{ct}) under dark and light and (**f**) shows device response time and recovery time are 21.8 ms and 29.9 ms, respectively. (**g**) Schematic of a device without subchannel layer in ionic liquid with 10% BMIMI. (**h**) EIS measurement shows charge-transfer-resistance (R_{ct}) under dark and light and (**i**) shows device response time and recovery time are 19.2 ms and 23.9 ms, respectively.

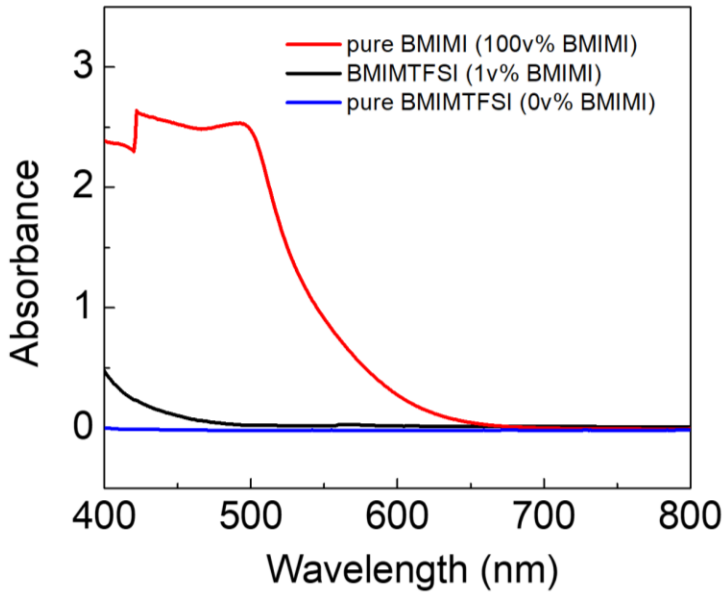

Extended Data Fig. 10 | Absorbance measurement of ionic liquid solvent (BMIMTFSI) and solvent mixed with different BMIMI concentration.

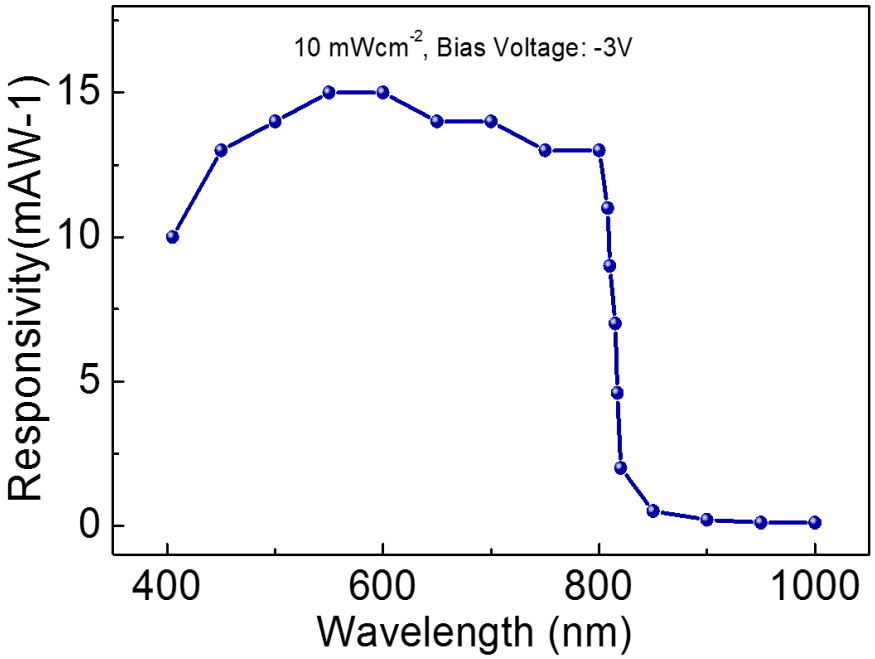

Extended Data Fig. 11 | Spectral response of individual pixel. The spectral responsivity was measured under the bias voltage of -3 V with a uniform light intensity of 10 $mWcm^{-2}$.

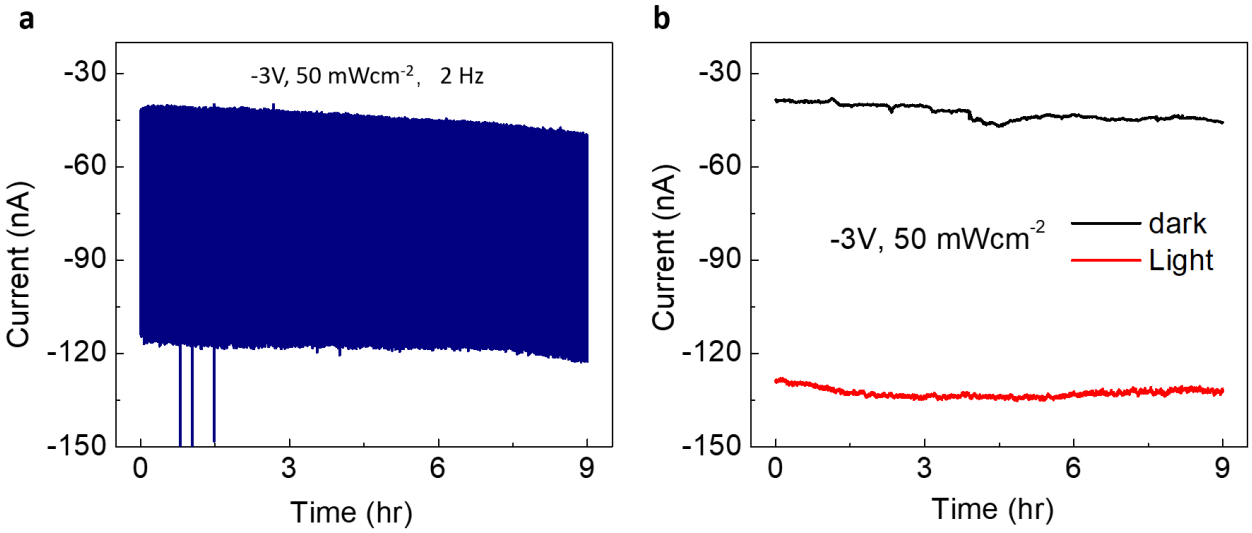

Extended Data Fig. 12 | The cycling (a) and reliability (b) tests of individual pixel under the bias of -3V and the illumination of solar simulator light, 50 $mWcm^{-2}$. This device was measured in ionic liquid mixed with 0.1% BMIMI concentration.

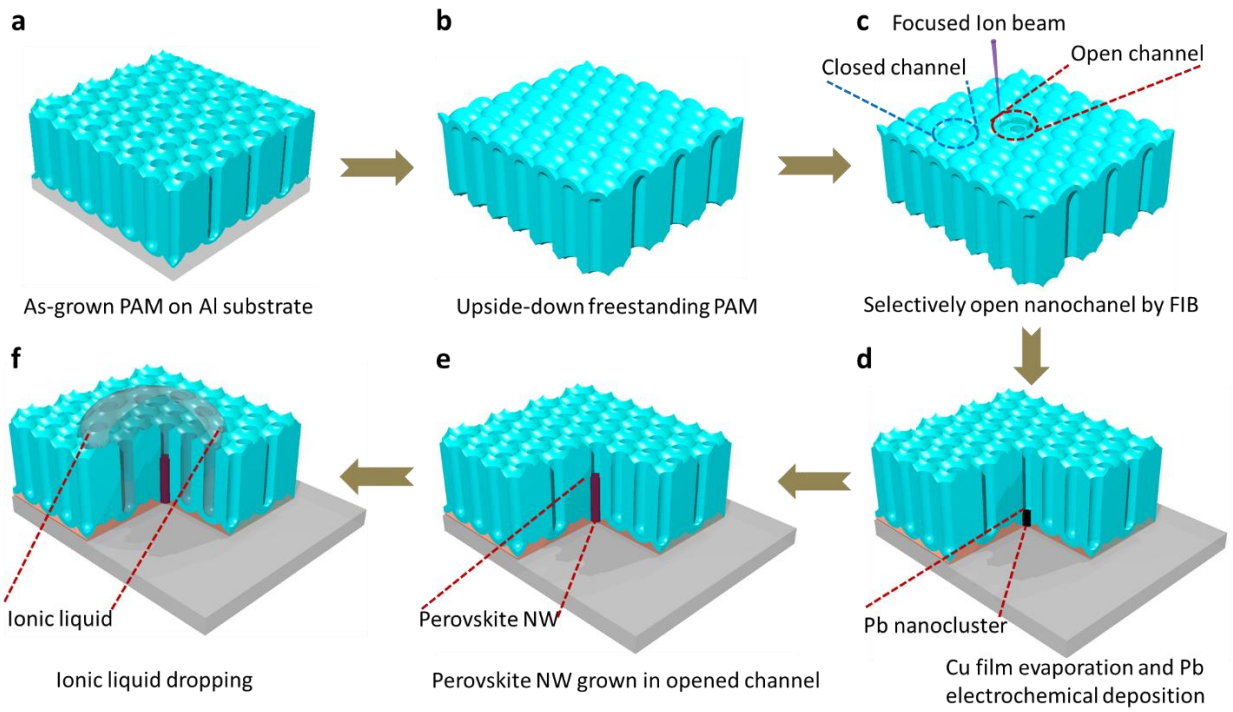

Extended Data Fig. 13 | Schematic fabrication process flow of a single NW based photodetector.

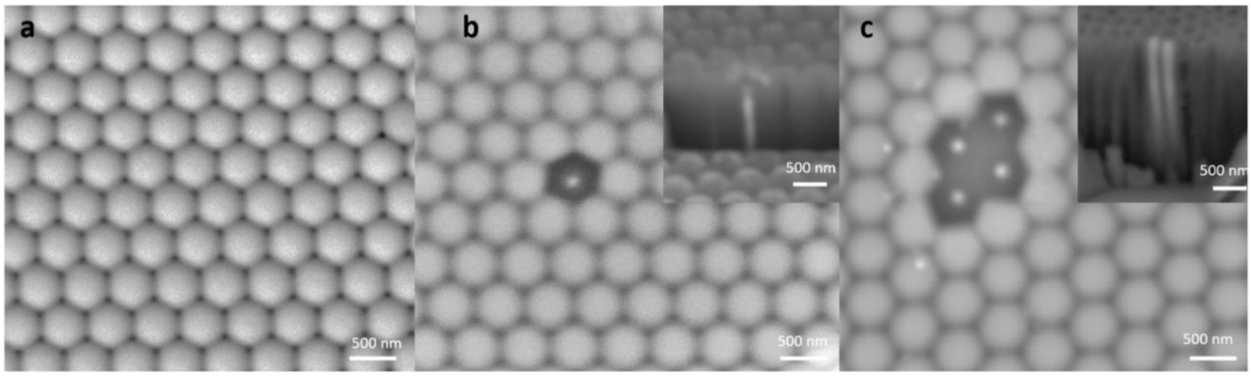

Extended Data Fig. 14 | Top and cross-sectional view SEM images of PAM at different stages: before FIB etching (**a**), with single nanowire filled (**b**) and with four nanowires filled (**c**).

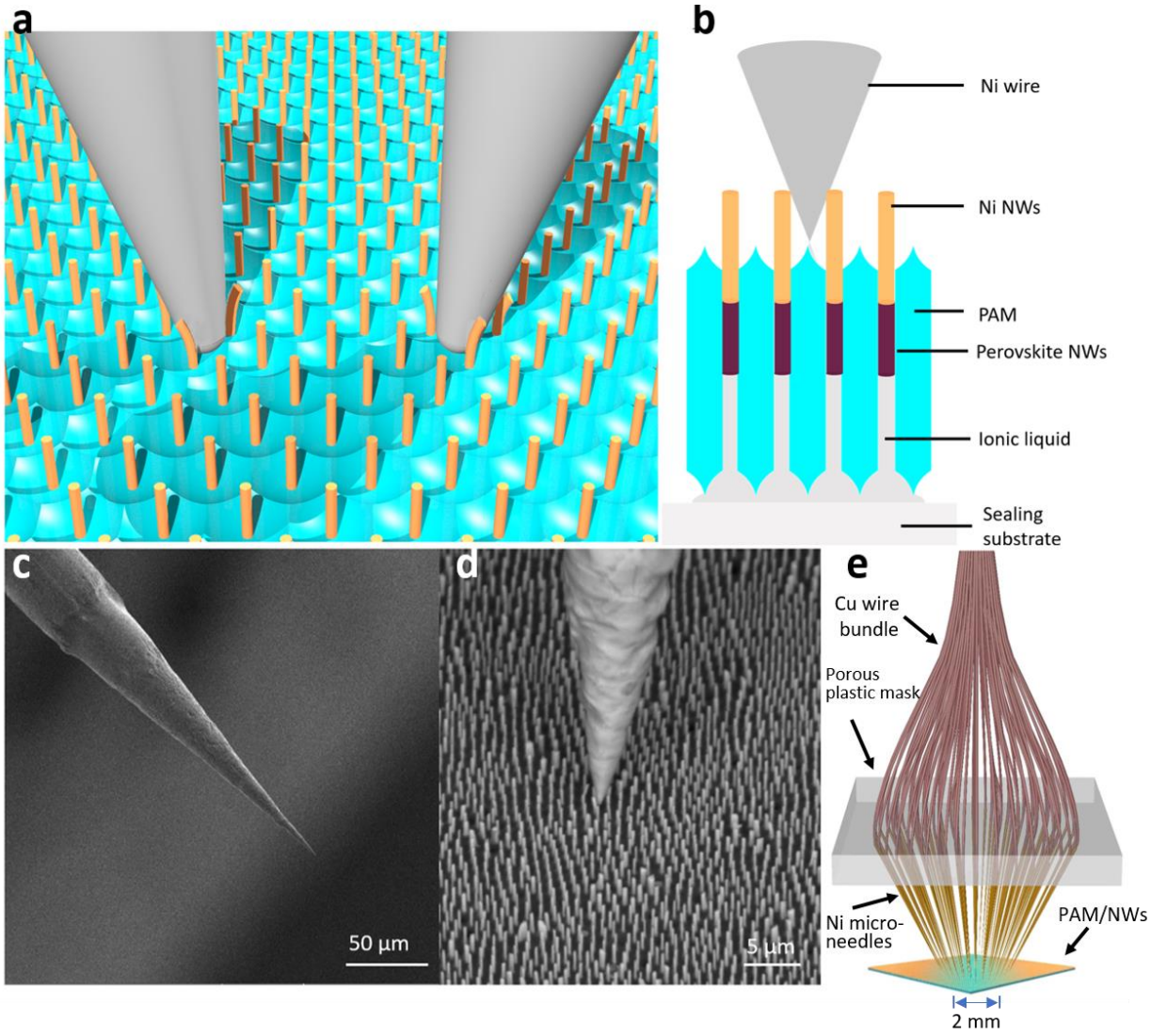

Extended Data Fig. 15 | Schematic of top (**a**) and cross-sectional view (**b**) of overall device structure. (**c**) SEM image of a sharpened Ni microwire (**d**) and the Ni microneedle inserted into Ni NW forest. (**e**) schematic of an assembled device with Ni microneedle array back contact on PAM.

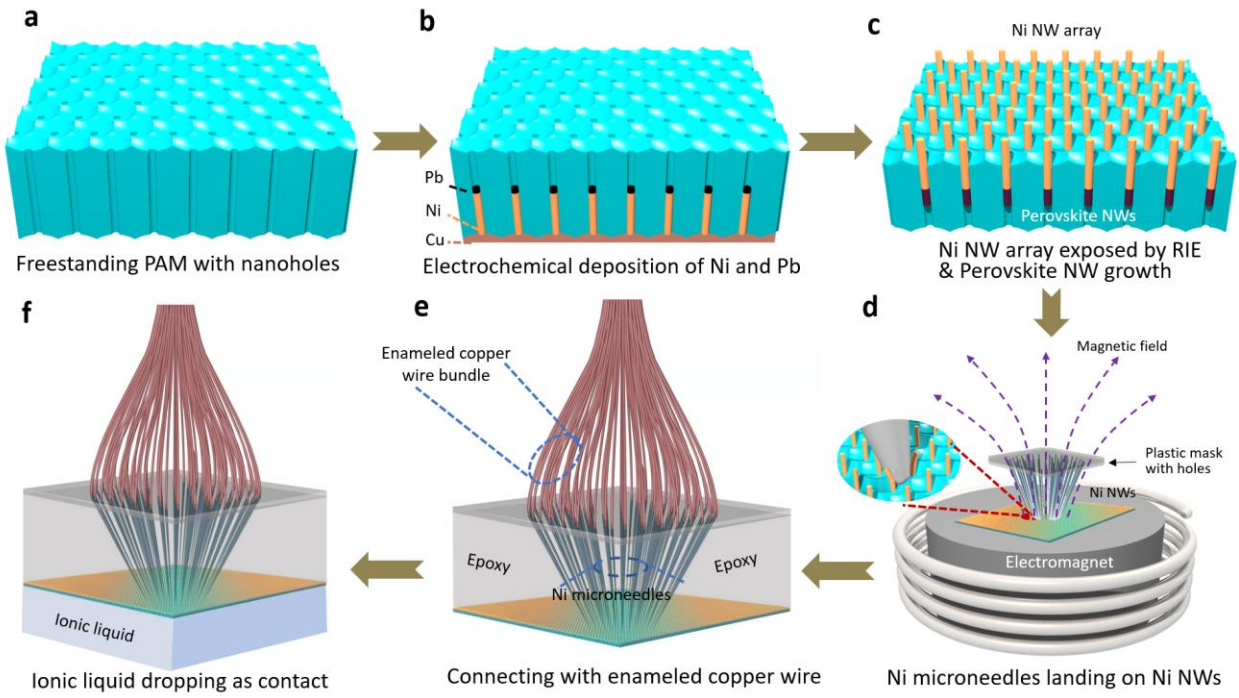

Extended Data Fig. 16 | Schematic fabrication process of integrated electrochemical image sensor based on microneedle array contacts assisted with magnetic field. (**a**) Freestanding PAM with through pores. (**b**) Pb and Ni NW grown in the PAM. (**c**) Perovskite NWs grown in the PAM and Ni NW exposed by RIE. (**d**) Magnetic field assisted assembly of Ni microwires on Ni NWs/PAM. (**e**) Epoxy packaged device. (**f**) Device with ionic liquid for measurement.

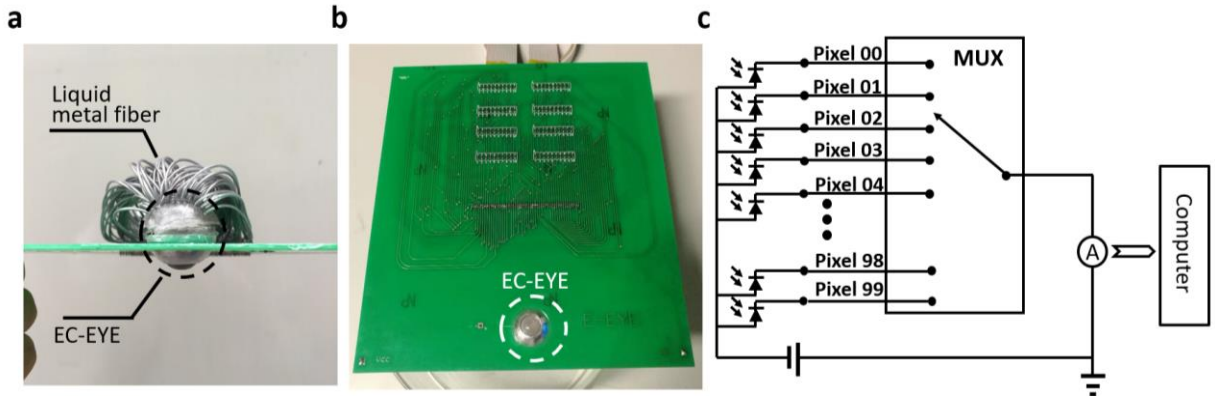

Extended Data Fig. 17 | Photos of EC-EYE mounted on PCB and measurement diagram. (**a**) The side-view and (**b**) front-view of EC-EYE mounted on PCB. (**c**) Circuit diagram of EC-EYE measurement setup.

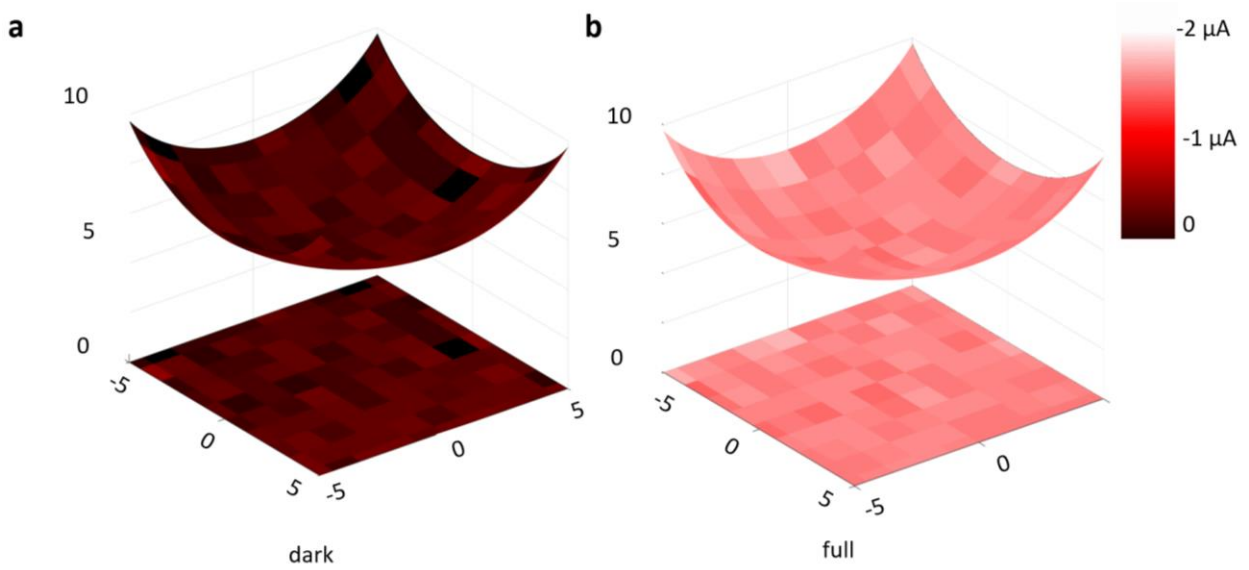

Extended Data Fig. 18 | Dark (**a**) and full-light (**b**) current mapping of EC-EYE. Full light: 0.5 sun (50 mWcm^{-2}) light from a solar simulator.

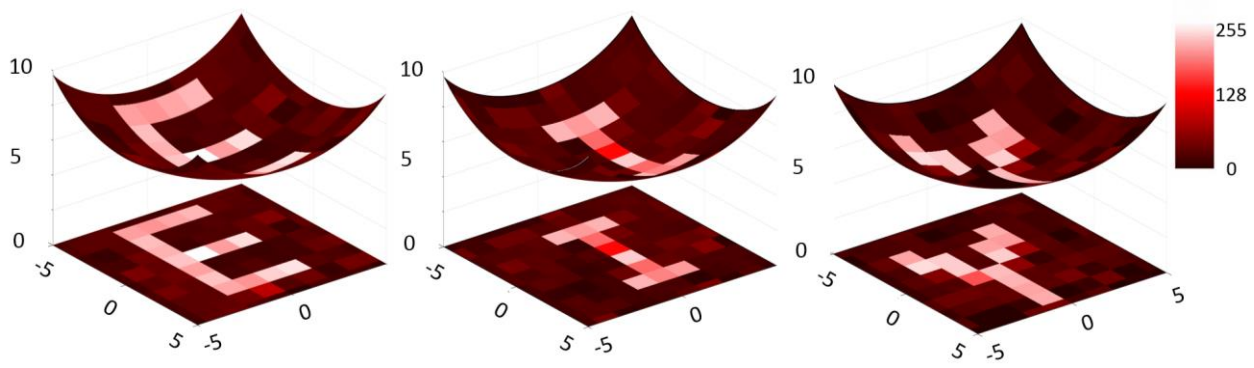

Extended Data Fig. 19 | Letters of "E", "I" and "Y" reconstructed by our EC-EYE imaging system.

To reconstruct the optical pattern projected on the image sensor, a photocurrent value was converted to grayscale number between 0 and 255. The formula used for grayscale conversion is the following:

$$G = (I_{Light} - I_{Dark})/(I_{Full} - I_{Dark}) \times 255$$

where G is the grayscale value, I_{Full}- I_{Dark} gives the dynamic range as the difference between the full light condition current and the dark current of a pixel. This is in fact the result of subtracting Extended Data Fig. 18a from Extended Data Fig. 18b.

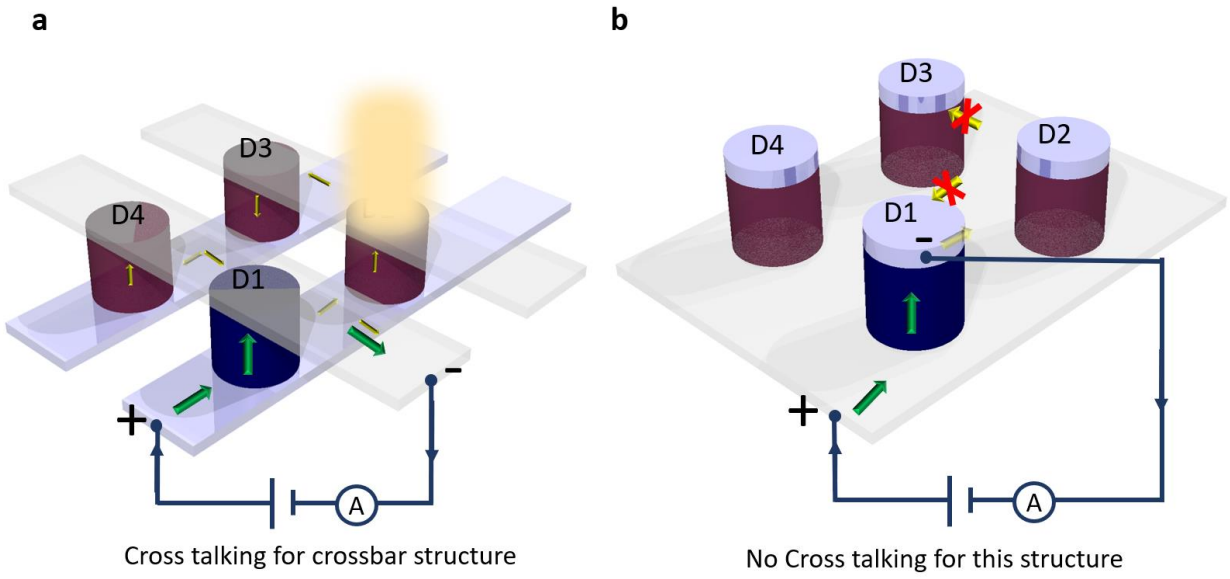

Extended Data Fig. 20 | Cross talking effect comparison of (**a**) crossbar structure and (**b**) our device structure.

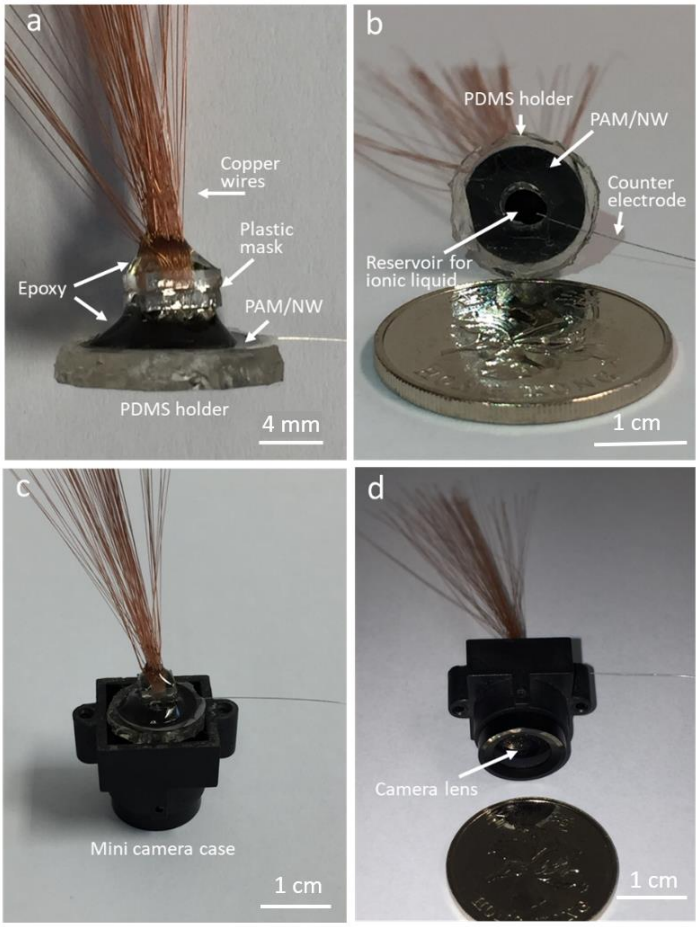

Extended Data Fig. 21 | Photos of fabricated perovskite NW EC image sensor on a PDMS holder and assembled with a mini-camera.

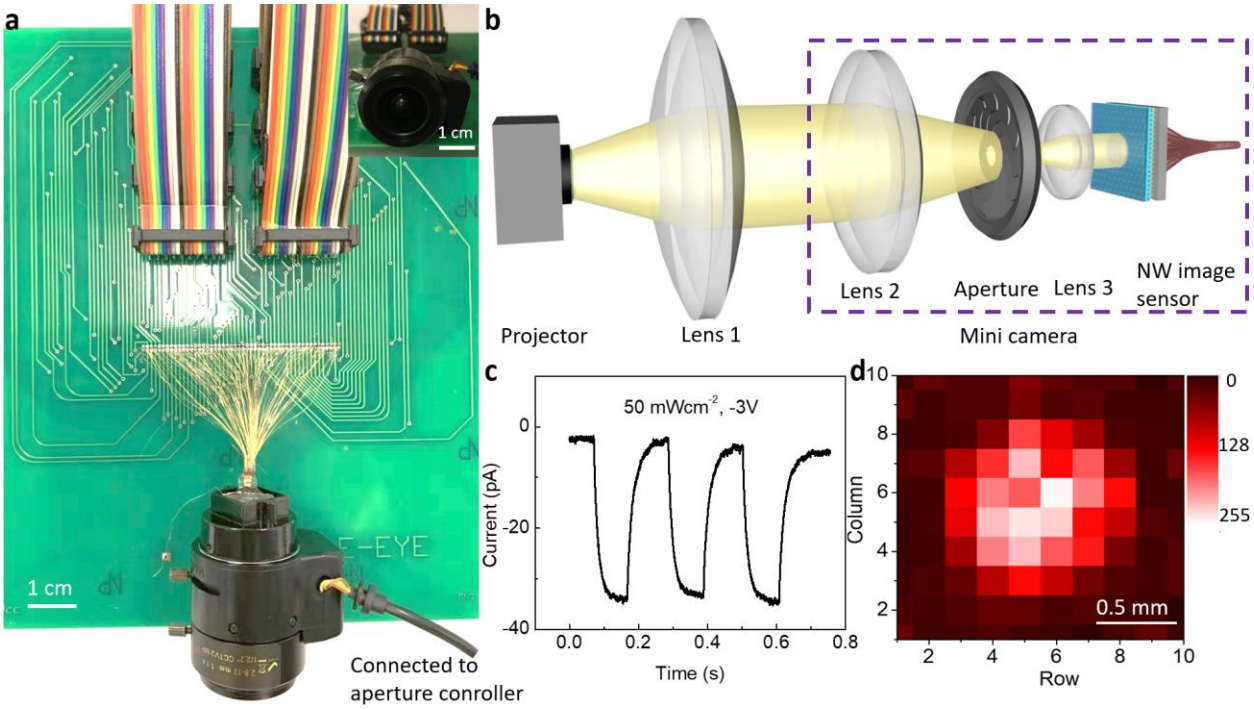

Extended Data Fig. 22 | (**a**) EC-EYE mounted on PCB. (**b**) Schematic of testing optical system. (**c**) Photoresponse of an individual pixel. (**d**) Image constructed from a light spot focusing on the 2 mm by 2 mm image sensor.

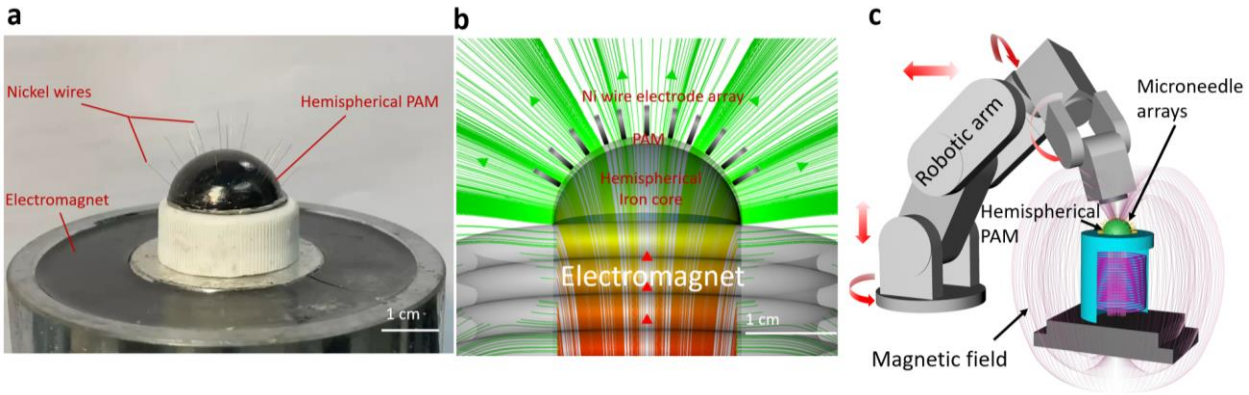

Extended Data Fig. 23 | Photo of 50 μm-diameter Ni microwires aligned on hemispherical PAM under magnetic field (**a**) and the calculated distribution of the field lines (**b**). (**c**) Schematic of automated Ni microneedles landing on hemispherical substrate. A video clip of Ni microwire alignment angle changing with varying the electromagnet input voltage is shown in Supplementary Movie 2.

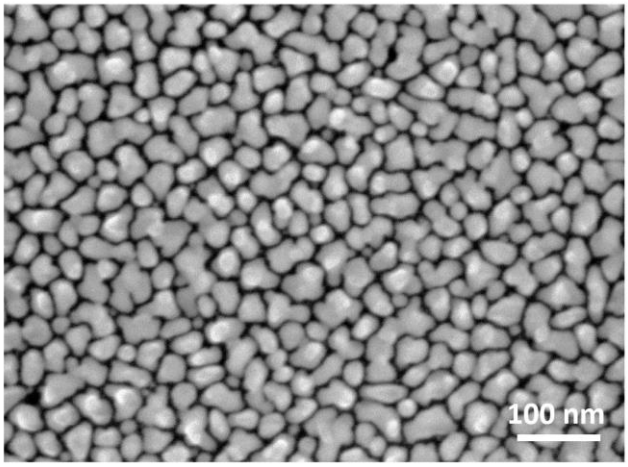

Extended Data Fig. 24 | The top-view SEM image of discontinuous indium layer evaporated at 1 $Å s^{-1}$ rate.

Materials	**Electrolyte**	**Peak responsivity (mAW^{-1})**	**Response/Recovery time (ms)**	**Reference**
$FAPbI_3$ NW	*BMIMTFSI (mixed with 10V% BMIMI)*	*303.2*	*19.2 /23.9*	*This work*
TiO_2 nanorods	H_2O	25	150 / 50	Ref 29
ZnO/ZnS coreshell	H_2O	56	40 / 40	Ref 30
ZnO nanorods	H_2O	21.3	20 / 20	Ref 30
ZnO nanowires	H_2O	110	150 / 500	Ref 31
Ag-ZnO nanowires	H_2O	370	140 / 520	Ref 31
TiO_2 nanotubes	0.1 M NaOH	11.2	200 / 200	Ref 32
SrO_3/TiO_2	0.1 M NaOH	18.6	200 /200	
InSe nanosheets	0.2 M KOH	0.0049	5000 / 6000	Ref 33
Black phosphorus	0.2 M KOH	0.0026	1000 / 1600	Ref 34
zZnO nanorods	$[Co(bpy)_3]^{3+/2+}$	3.95	~ 200 / 200	Ref 35
ZnO film	0.5 M Na_2SO_4	0.05	110 / 210	Ref 36
PbOx nanosheets	BMIMCl	22	NA / NA	Ref 37
	$BMIMPF_6$	25	NA / NA	
	$BMIMTF_2N$	44	NA / NA	
SnO_2 nanofiber/ TiO_2 branches	I^-/I_3^-	22.5	30 / 10	Ref 38
SnO_2/TiO_2 microtubes	I^-/I_3^-	64.5	~100 / 200	Ref 39
TiO_2 Nanorods cloth/nanorods	I^-/I_3^-	152	300 / 200	Ref 40
WSe_2	1M H_2SO_4	0.4	NA / NA	Ref 41

Extended Data Table 1 | Comparison of photodetection performance of EC-EYE with photoelectrochemical photodetectors in literature.

Calculation of Photon Flux Received by a Single NW

The number of photons on individual NW can be calculated by the formula of $n = (P \times S)/(h\nu)$, where *P, S, h* and *ν* represent the incident power, nanowire cross-section area, Planck constant and average light frequency, respectively. Under the lowest radiation level measured, which is ~ 0.3 μWcm^{-2}, the number of photons received by individual nanowire can be estimated as 23 photons per second.

Calculation of the Detectivity of an Individual Pixel

The specific detectivity is calculated by the formula of $D^* = A^{1/2}R/(2qI_{dark})^{1/2}$, where R is the responsivity, A is the effective area of the detector, q is the absolute value of electron charge, and I_{dark} is the dark current. Under the lowest radiation level measured, which is ~ 0.3 μWcm^{-2}, the specific detectivity is calculated as ~2.7×10^9 Jones.